NAVAL POSTGRADUATE SCHOOL

MONTEREY, CALIFORNIA

THESIS

EVALUATION OF MATCHED-FIELD PROCESSING TECHNIQUES USING SIMULATED ACOUSTIC VECTOR SENSOR DATA

by

Yu-Chih Hsu

December 2005

Thesis Advisor:	Kevin B. Smith
Second Reader:	Daphne Kapolka

THIS PAGE INTENTIONALLY LEFT BLANK

REPORT DOCUMENTATION PAGE			Form Approved OMB No. 0704-0188
Public reporting burden for this collection of information is estimated to average 1 hour per response, including the time for reviewing instruction, searching existing data sources, gathering and maintaining the data needed, and completing and reviewing the collection of information. Send comments regarding this burden estimate or any other aspect of this collection of information, including suggestions for reducing this burden, to Washington headquarters Services, Directorate for Information Operations and Reports, 1215 Jefferson Davis Highway, Suite 1204, Arlington, VA 22202-4302, and to the Office of Management and Budget, Paperwork Reduction Project (0704-0188) Washington DC 20503.			
1. AGENCY USE ONLY *(Leave blank)*	**2. REPORT DATE** December 2005	**3. REPORT TYPE AND DATES COVERED** Master's Thesis	
4. TITLE AND SUBTITLE: Evaluation of Matched-Field Processing Techniques using Simulated Acoustic Vector Sensor Data			**5. FUNDING NUMBERS**
6. AUTHOR(S) Yu-Chih Hsu			
7. PERFORMING ORGANIZATION NAME(S) AND ADDRESS(ES) Naval Postgraduate School Monterey, CA 93943-5000			**8. PERFORMING ORGANIZATION REPORT NUMBER**
9. SPONSORING /MONITORING AGENCY NAME(S) AND ADDRESS(ES) N/A			**10. SPONSORING/MONITORING AGENCY REPORT NUMBER**
11. SUPPLEMENTARY NOTES The views expressed in this thesis are those of the author and do not reflect the official policy or position of the Department of Defense or the U.S. Government.			
12a. DISTRIBUTION / AVAILABILITY STATEMENT Approved for public release; distribution is unlimited.			**12b. DISTRIBUTION CODE**

13. ABSTRACT (maximum 200 words)

There has recently been growing interest in the use of acoustic particle velocity measurements for sonar system applications such as source localization. It is expected that acoustic particle velocity sensors or "vector" sensors have the potential to improve the performance of scalar acoustic pressure sensors. Although extensive research has been performed to study the enhancements for plane-wave beamforming, little has been done in the more general area of matched-field processing. Some researchers maintain that the collective performance of pressure sensors in an array is equivalent to that of vector sensors, i.e. measuring the three components of acoustic particle velocity in addition to pressure; however, this position has not been proven conclusively. This thesis serves to provide insight into possible improvements in matched-field processing performance realizable through the use of vector sensors. First, a proven numerical method is used to simulate an acoustic field. The field observed at an array of vector sensors and their predicted replica fields are correlated in order to localize a continuous-wave point source at an arbitrary (but known) depth and distance. The comparison of performance is carried out using an Ambiguity Surface, as is typically done in linear (Bartlett) matched-field processing techniques, at 1000 Hz. The level of performance is further evaluated in the presence of different environments, source positions and perturbations. Through the use of the developed matched-field processor verified with known theory, this thesis concluded that the performance of a vector sensor array is not clearly superior to a hydrophone array of similar specifications. In the environments investigated, no improvement in performance was demonstrated for the vector sensor array over that expected for an array consisting of pressure sensors alone.

14. SUBJECT TERMS Matched-Field Processing, Acoustic Particle Velocity, Beamforming, MMPE			**15. NUMBER OF PAGES** 91
			16. PRICE CODE
17. SECURITY CLASSIFICATION OF REPORT Unclassified	**18. SECURITY CLASSIFICATION OF THIS PAGE** Unclassified	**19. SECURITY CLASSIFICATION OF ABSTRACT** Unclassified	**20. LIMITATION OF ABSTRACT** UL

NSN 7540-01-280-5500 Standard Form 298 (Rev. 2-89)
Prescribed by ANSI Std. 239-18

THIS PAGE INTENTIONALLY LEFT BLANK

Approved for public release; distribution is unlimited

EVALUATION OF MATCHED-FIELD PROCESSING TECHNIQUES USING SIMULATED ACOUSTIC VECTOR SENSOR DATA

Yu-Chih Hsu
Major, Republic of Singapore Navy
B.S., United States Naval Academy, 1996

Submitted in partial fulfillment of the
requirements for the degree of

MASTER OF SCIENCE IN COMBAT SYSTEMS TECHNOLOGY

from the

NAVAL POSTGRADUATE SCHOOL
December 2005

Author: Yu-Chih Hsu

Approved by: Kevin B. Smith
Thesis Advisor

Daphne Kapolka
Second Reader

James H. Luscombe
Chairman, Department of Physics

THIS PAGE INTENTIONALLY LEFT BLANK

ABSTRACT

There has recently been growing interest in the use of acoustic particle velocity measurements for sonar system applications such as source localization. It is expected that acoustic particle velocity sensors or “vector” sensors have the potential to improve the performance of scalar acoustic pressure sensors. Although extensive research has been performed to study the enhancements for plane-wave beamforming, little has been done in the more general area of matched-field processing. Some researchers maintain that the collective performance of pressure sensors in an array is equivalent to that of vector sensors, i.e. measuring the three components of acoustic particle velocity in addition to pressure; however, this position has not been proven conclusively. This thesis serves to provide insight into possible improvements in matched-field processing performance realizable through the use of vector sensors. First, a proven numerical method is used to simulate an acoustic field. The field observed at an array of vector sensors and their predicted replica fields are correlated in order to localize a continuous-wave point source at an arbitrary (but known) depth and distance. The comparison of performance is carried out using an Ambiguity Surface, as is typically done in linear (Bartlett) matched-field processing techniques, at 1000 Hz. The level of performance is further evaluated in the presence of different environments, source positions and perturbations. Through the use of the developed matched-field processor verified with known theory, this thesis concluded that the performance of a vector sensor array is not clearly superior to a hydrophone array of similar specifications. In the environments investigated, no improvement in performance was demonstrated for the vector sensor array over that expected for an array consisting of pressure sensors alone.

THIS PAGE INTENTIONALLY LEFT BLANK

TABLE OF CONTENTS

LIST OF FIGURES

THIS PAGE INTENTIONALLY LEFT BLANK

LIST OF TABLES

THIS PAGE INTENTIONALLY LEFT BLANK

ACKNOWLEDGMENTS

To God and my Lord Jesus Christ for leading me and providing for everything. To my lovely wife, Edna, who took such good care of my home and family that I was able to concentrate in my academic requirements.

To Professor Kevin Smith for his kind guidance and patience every step of the way, making the completion of this thesis possible. Also to Professor Daphne Kapolka, not just for her helpful pointers, but also for taking such great care of the Singaporean sensor students including myself when we first arrived at NPS, continuing to render encouragement and assistance even after being relieved in her responsibility to do so.

Last but no least, to my two lovely daughters, Joelle and Ashley, who were my source of joy and motivation.

THIS PAGE INTENTIONALLY LEFT BLANK

I. INTRODUCTION

Interest in the vector particle velocity fields associated with the propagation of underwater acoustic energy has been rising in the past decade, especially with the possibilities of improving sonar system performance through the measurement of particle velocity in addition to the traditional pressure measurement. With information from the three dimensions of particle velocity added to the scalar pressure at the same point, one would expect the combined information to be more useful than that of pressure alone. However, as in most cases, hydrophones are typically not used singly, but in numbers as part of an array. An array of hydrophones can localize noise sources fairly accurately (depending on the array length, element spacing, and environment), as the numerous hydrophones not only provide individual pressure information, but also allow one to determine the direction of a source using the phase difference between the elements of the array.

Limits of system performance have been thoroughly examined analytically ([1] and [2]). But little experimental data exists to provide true, empirical evidence of system improvements between identical arrays of either pressure or vector (pressure and velocity) sensors. Numerical calculations that can provide “realistic” structure in the presence of oceanographic variability are then useful tools.

The objective of this thesis is to examine the difference in performance between hydrophone arrays and Acoustic Vector Sensor (AVS) arrays (measuring pressure and particle velocity). This was done by developing a matched field processor that correlates the field observed at the array of sensors with their predicted replica fields. The acoustic fields were simulated by a proven model based on Parabolic Equation (PE).

A. BACKGROUND

In order for acoustic particle velocity (or its components) to be beneficial for underwater localization, its application has to improve localization performance beyond that of simply using scalar pressure measurements through hydrophones or to achieve comparable performance with fewer sensors. To better evaluate this possibility, it is important to first understand the basic relationship between pressure and acoustic particle velocity. Some known standard equations are shown below.

Assuming linear wave acoustics, the linearized Euler's equation can be derived from Newton's 2nd Law for fluids [3] as

$$\rho_0 \frac{\partial \vec{v}}{\partial t} = -\vec{\nabla} p \ , \tag{1.1}$$

where ρ_0 is the density at equilibrium, $\vec{v}$ is the vector particle velocity and p is the acoustic pressure. Consider plane wave propagation at angular frequency, ω, in the x-direction over time t. In this case, the pressure is given by

$$p = Ae^{i(kx-\omega t)} \ , \tag{1.2}$$

where A is an arbitrary constant representing the amplitude of the pressure.

From the equation of state, it can be derived that

$$p = \rho_0 c^2 s \Rightarrow s = \frac{p}{\rho_0 c^2} = \frac{A}{\rho_0 c^2} e^{i(kx-\omega t)} \ , \tag{1.3}$$

where s stands for the condensation, $\frac{\rho - \rho_o}{\rho_o}$, and c for speed of sound. Applying the linearized Euler's equation, an expression for particle velocity can be derived as

$$\rho_0 i\omega v = ikp \Rightarrow v = \frac{p}{\rho_0 c} = \frac{A}{\rho_0 c} e^{i(kx-\omega t)} \ , \tag{1.4}$$

indicating that pressure and particle velocity are in phase for traveling plane waves.

For a spherical wave, the particle velocity is given by

$$\vec{v} = \frac{r}{\rho_0 c}\left(1 - \frac{i}{kr}\right) p \ , \tag{1.5}$$

where k is the wave number and r is an arbitrary distance from the origin. Equation (1.5) implies that pressure and particle velocity are out of phase, though where $kr \gg 1$, i.e. distance (r) is far greater than the wavelength (λ), the relationship between pressure and particle velocity becomes similar to that of plane waves.

The above equations show that for most cases (where $kr \gg 1$), pressure and acoustic particle velocity are in phase.

B. PAST WORK AND RECENT DEVELOPMENTS

There has been a lot of recent interest in the uses of acoustic particle velocity for various purposes including the localization of acoustic sources of interest. Acoustic Vector Sensors have already been constructed and tested at sea. They measure the acoustic pressure and all three orthogonal components of the acoustic particle velocity (or a related quantity, for example, acceleration) at a single point in space. Hawkes and Nehorai [1] proposed that these sensors, and arrays composed of them, have a number of advantages over traditional hydrophone arrays, such as:

- "Improved performance for a given aperture"
- "Full azimuth/elevation estimation with a linear array (or even a single AVS)"
- "Can be used in a sparse (undersampled) configuration with uniform geometry"

Cray and Nuttall [5] added from a theoretical point of view using directivity as comparison that even a single uniaxial velocity sensor can have a maximum directivity 3 times (or 4.8 dB) greater than an omnidirectional pressure sensor, though not for all signal arrival angles. For an AVS that measures all components of particle velocity as well as scalar pressure, it has a maximum directivity 4 times (or 6 dB) that of the pressure sensor.

D'Spain, Hodgkiss and Edmonds [6] offer a different point of view. They believe that the use of acoustic particle velocity alone as a measure of the directionality of the sound field cannot be depended upon. Instead, they believe that it is the time-averaged acoustic intensity vector that provides the physically meaningful measure of both the magnitude and direction of acoustic propagation.

In agreement, Smith [7] states that an array of pressure sensors appropriately spaced would provide the same information as that of a similar AVS array. Furthermore, any single sensor (pressure or AVS) would not be able to distinguish arrival angles in the presence of multipath interference, but would still require an array of sensors.

C. THESIS OUTLINE

This thesis seeks to investigate the performance of a simple, linear correlation processor applied to the acoustic field using either just pressure or a combination of pressure and particle velocity. Theoretical analyses will be conducted using MATLAB codes to investigate the performance of this processor.

The Monterey-Miami Parabolic Equation (MMPE) model [6] employed to compute the acoustic vector field quantities is described in Chapter II. This model propagates in range the predicted solutions of the acoustic pressure field using the Split-Step Fourier (SSF) method. Particle velocity is then computed locally based on vertical and horizontal derivatives of the local field. Various source/receiver geometries and environmental characterizations can then be studied.

Chapter III explains the data processing techniques used in this thesis. There were two types of processing techniques used. Beamforming Techniques were designed to test the developed correlation processor against known theory in order to verify its validity. Matched-Field Processing Techniques were then implemented to compare the performance of pressure sensor arrays and AVS arrays through the use of Ambiguity Surfaces. The variability and intensity of the Ambiguity Surfaces provide an indication of the ability of an array to resolve the location of a known source.

Chapter IV provides details such as the various parameters and procedures used in the process of conducting the Matched-Field Processing (MFP) techniques mentioned

above. The results from these techniques, and the summary and evaluation of results are also presented in this chapter.

Chapter V presents the conclusions of this thesis and possible future work that can further this area of research.

THIS PAGE INTENTIONALLY LEFT BLANK

II. MONTEREY-MIAMI PARABOLIC EQUATION MODEL

A. THEORY AND BASIC NUMERICAL IMPLEMENTATION

The Monterey-Miami Parabolic Equation (MMPE) model is a numerical model developed by Smith and Tappert [8]. It has since been further refined by Smith and was the primary tool used in this thesis to simulate the acoustic field. The following is a brief description of how MMPE simulates the acoustic vector field based on [7], [9] and [10].

1. Basic Theory

Assume that the time-harmonic acoustic field in a cylindrical coordinate system is represented by

$$P(r,z,\varphi,\omega t) = p(r,z,\varphi)e^{-i\omega t} \ . \tag{2.1}$$

Substituting this into the linearized acoustic wave equation in cylindrical coordinates leads to the Helmholtz equation,

$$\frac{1}{r}\frac{\partial}{\partial r}\left(r\frac{\partial p}{\partial r}\right)+\frac{1}{r^2}\frac{\partial^2 p}{\partial \varphi^2}+\frac{\partial^2 p}{\partial z^2}+k_0^2 n^2\left(r,z,\varphi\right)p=-4\pi P_0\delta\left(\vec{x}-\vec{x}_s\right), \tag{2.2}$$

where $k_0=\dfrac{\omega}{c_0}$ is the reference wavenumber, $n\left(r,z,\varphi\right)=\dfrac{c_0}{c(r,z,\varphi)}$ is the acoustic index of refraction, c_0 is the reference sound speed, and $c(r,z,\varphi)$ is the acoustic sound speed. All features of the environment are represented within $c(r,z,\varphi)$. The source function is that of a point source at coordinates $\left(r=0,z=z_s\right)$ with reference source level P_0 defined as the pressure amplitude at a reference distance of $R_0=1$ m, and

$$\delta\left(\vec{x}-\vec{x}_s\right)=\frac{1}{2\pi r}\delta\left(z-z_s\right)\delta\left(r\right) \tag{2.3}$$

is the Dirac-delta function defining the point source contribution. To account for the cylindrical spreading, $p\left(r,z\right)=\dfrac{1}{\sqrt{r}}u\left(r,z\right)$ is defined, which for the homogeneous equation yields

$$\frac{\partial^2 u}{\partial r^2}+\frac{1}{r^2}\frac{\partial^2 u}{\partial \varphi^2}+\frac{\partial^2 u}{\partial z^2}+k_0^2\left(n^2+\frac{1}{4k_0^2 r^2}\right)=0\,. \tag{2.4}$$

The final term in this equation drops off like $\frac{1}{r^2}$ and is generally neglected in the solution. The second term in this equation introduces azimuthal coupling between different radials, and is generally small. The neglecting of this term is often referred to as the Uncoupled Azimuth (UNCA) Approximation.

The remaining Helmholtz equation can then be factored by introducing the operator notation

$$P_{op}=\frac{\partial}{\partial r}, \qquad Q_{op}=\left(\mu+\varepsilon+\nu+1\right)^{\frac{1}{2}}\,, \tag{2.5}$$

where

$$\varepsilon=n^2-1, \qquad \mu=\frac{1}{k_0^2 r^2}\frac{\partial^2}{\partial z^2}, \qquad \nu=\frac{1}{k_0^2 r^2}\frac{\partial^2}{\partial \varphi^2}\,.$$

This thesis assumes azimuthal symmetry, hence the ν term is zero. The commutator $\left[P_{op},Q_{op}\right]$ is assumed negligible, implying weak range dependence in the environment, and is, in fact, exactly zero in layered media. The outgoing wave then satisfies

$$P_{op}\Psi=ik_0 Q_{op}\Psi \tag{2.6}$$

or $$-ik_0^{-1}\frac{\partial\Psi}{\partial r}=Q_{op}\Psi\,.$$

When backscattered energy is negligible, this represents the complete description of the forward propagating acoustic energy in the waveguide, and is the foundation for all underwater acoustic parabolic equation (PE) models. The generation of solutions depends partly on developing approximations to the pseudo-differential operator Q_{op}. It should be noted that if a slowly-modulating function is introduced by defining $\Psi=\psi e^{ik_0 r}$, the PE takes the form

$$\frac{\partial\psi}{\partial r}=ik_0\left[Q_{op}-1\right]\psi \quad . \tag{2.7}$$

From Eq. (2.7) above, the general form of the parabolic approximation to the Helmholtz wave equation for acoustic pressure can be defined

$$\frac{\partial \psi}{\partial r} = -ik_0\left(1-Q_{op}\right)\psi = -ik_0 H_{op}\psi, \tag{2.8}$$

where ψ is the PE field function, defined by

$$p\left(\vec{r}\right) = P_0\sqrt{\frac{R_0}{r}}\psi\left(\vec{r}\right)e^{ik_0 r} \ . \tag{2.9}$$

This analysis is focused on implementation using the Split-Step Fourier (SSF) technique [11] which is purely for convenience. The calculation of the velocity field will depend upon operations that are easily performed using Fourier transforms, and the PE model to be employed already utilizes the SSF algorithm. The SSF algorithm requires a separation of the operator

$$H_{op} = T_{op} + U_{op} + V_{op} \ . \tag{2.10}$$

It shall be assumed that the uncoupled azimuth approximation is valid, and all motion is in the (r,z) plane. Then, $v = 0$ and its associated operator V_{op} also vanishes. The WAPE by Thomson and Chapman [12] approximation is used here. Then

$$T_{op} = 1-\left[1+\frac{1}{k_0^2}\frac{\partial^2}{\partial z^2}\right] \tag{2.11}$$

$$U_{op} = -\left(n-1\right)+U\left(\rho\right) \ . \tag{2.12}$$

Using the convention

$$\psi\left(z\right) = FFT\left[\hat{\psi}\left(k_z\right)\right] \text{ and } \hat{\psi}\left(z\right) = IFFT\left[\psi\left(k_z\right)\right] \ , \tag{2.13}$$

then

$$T_{op}\left(\frac{\partial^2}{\partial z^2}\right)\psi\left(z\right) = FFT\left\{\hat{T}_{op}\left(-k_z^2\right)\bullet IFFT\left[\psi\left(z\right)\right]\right\} \ , \tag{2.14}$$

where $\hat{T}_{op}\left(k_z^2\right)$ is now simply a scalar operator defined by

$$\hat{T}_{op}\left(k_z^2\right)=1-\left[1-\left(\frac{k_z}{k_0}\right)^2\right]^{1/2} \quad . \tag{2.15}$$

The evolution of the PE field function then satisfies the SSF algorithm according to

$$\psi\left(r+\Delta r,z\right)=e^{-ik_0\frac{\Delta r}{2}U_{op}\left(r+\Delta r,z\right)}FFT\left\{e^{-ik_0\Delta r\hat{T}_{op}\left(k_z\right)}IFFT\left[e^{-ik_0\frac{\Delta r}{2}U_{op}\left(r,z\right)}\psi\left(r,z\right)\right]\right\} \quad . \tag{2.16}$$

2. Calculating Acoustic Particle Velocity Fields from a Parabolic Equation Model

This is work done by Smith, taken from [7]. By conservation of linear momentum, the acoustic particle velocity, $\vec{v}=\left(v_r,v_z\left(v_\phi\right)\right)$, is related to the pressure by

$$\vec{v}=-\frac{i}{\omega\rho_0}\nabla p \quad , \tag{2.17}$$

assuming both $\vec{v}$ and p have the same e^{-iwt} time dependence. In cylindrical coordinates, this becomes

$$\vec{v}=-\frac{i}{\omega\rho_0}\left[\frac{\partial}{\partial r}\hat{r}+\frac{\partial}{\partial z}\hat{z}\right] . \tag{2.18}$$

Separating the components,

$$\begin{aligned} v_r &= -\frac{i}{\omega\rho_0}P_0R_0^{1/2}\left[-\frac{1}{2r^{3/2}}+\frac{ik_0}{r^{1/2}}+\frac{1}{r^{1/2}}\frac{\partial\psi}{\partial r}\right] \\ &= \frac{P_0}{c_0\rho_0}\sqrt{\frac{R_0}{r}}e^{ik_0r}\left[\left(\frac{i}{2k_0r}+1\right)\psi-H_{op}\psi\right] \end{aligned} \quad . \tag{2.19}$$

Applying Eqs. (2.10)-(2.12), this becomes

$$v_r\left(r,z\right)=\frac{P_0}{c_0\rho_0}\sqrt{\frac{R_0}{r}}e^{ik_0r}\left[\left(n-U_{op}\left(\rho\right)+\frac{i}{2k_0r}\right)\psi\left(r,z\right)-T_{op}\psi\left(r,z\right)\right] , \tag{2.20}$$

where the application of the operator is achieved by invoking Eq. (2.14). In the vertical plane,

$$v_z = -\frac{iP_0}{\omega\rho_0}\sqrt{\frac{R_0}{r}}e^{ik_0 r}\frac{\partial\psi}{\partial z}\ , \tag{2.21}$$

which can be solved using the FFT technique, i.e.,

$$v_z\left(r,z\right) = \frac{P_0}{c_0\rho_0}\sqrt{\frac{R_0}{r}}e^{ik_0 r}FFT\left[\frac{ik_z}{k_0}IFFT\left(\psi\left(r,z\right)\right)\right]\ . \tag{2.22}$$

THIS PAGE INTENTIONALLY LEFT BLANK

III. DATA PROCESSING TECHNIQUES

A. INTRODUCTION

Two types of data processing techniques were developed for this thesis. The purpose of the Beamforming Techniques was mainly to establish the validity of the core program which formed the basis of the later matched-field processor based on [5]. This provides confidence that the processor is working according to expectations and could, therefore, be applied to the Matched-Field Processing Techniques, the actual techniques required for this thesis. It is important to emphasize again that this thesis assumed azimuthal symmetry. Further elaborations on both techniques are provided below.

B. BEAMFORMING TECHNIQUES

Three Beamforming Techniques were designed in order to show that the correlation processor developed conforms to the theory based on [5], i.e. that an AVS array has a higher directivity than a pressure array. AVS array data was expected to provide up to a maximum improvement of 6 dB for the 2-D propagation considered for this thesis. To show the improvement, the three Beamforming Techniques were designed to be similar except for the weights used to combine the various sensor components on a vertical array of sensors. The varied sets of weightings used were as follow:

- pressure only;
- equal weighting between pressure, horizontal and vertical components of particle velocity;
- optimal weighting of (1:3:3) for pressure, horizontal and vertical components of particle velocity, respectively, as derived in [5].

1. Theory

The replica needed for the beamformer processor was simulated by the simple plane-wave arrival,

$$R_{pn} = e^{i\vec{k}\bullet\vec{r}_n} = e^{iknd\sin\phi} \quad , \tag{3.1}$$

where p stands for pressure, assumed incident on the array at angle ϕ (relative to broadside), n for the number of elements in the array, and d for the distance between the elements.

The replicas for the horizontal and vertical components of particle velocity were similarly represented by a plane-wave phase along the array, i.e.

$$R_{v_r n} = R_{v_z n} = R_{pn} = e^{i\vec{k}\bullet\vec{r}_n} \quad , \tag{3.2}$$

where v_r and v_z stand for the horizontal and vertical components of particle velocity, respectively. Note that for a simple, plane-wave beamformer, all replicas are the same since they merely provide information of the relative phase along the array.

The measured data was derived from the general linear processor defined in [5],

$$B^{(pv)}(\theta,\phi) = \left| \sum_n \left(\vec{w}_n \bullet \vec{v}_n + w_{pn} v_{pn} \right) e^{-i\vec{k}_s \bullet \vec{r}_n} \right|^2 \tag{3.3}$$

where $\vec{v}_n = \vec{V}_n e^{i\vec{k}\bullet\vec{r}_n}$, $v_{pn} = V_{pn} e^{i\vec{k}\bullet\vec{r}_n}$, $V_{pn} = \dfrac{P_n}{\rho c}$ and $\vec{k}_s \bullet \vec{r}_n = kz_n \sin\phi_s$.

This expression can be simplified assuming equal weighting across components to

$$B^{(pv)}(\phi_s) = \left| \sum_n \left(w_{rn} v_{rn} + w_{zn} v_{zn} + w_{pn} v_{pn} \right) e^{-i\vec{k}_s \bullet \vec{r}_n} \right|^2 \quad , \tag{3.4}$$

where the weights $w_{rn} = w_n \cos\phi_s$, $w_{zn} = w_n \sin\phi_s$, and $w_{pn} = w_n$. Note that this steers all vector elements to the beamformer look direction, ϕ_s. The array element weights, w_n, can be defined by standard window functions such as the Hanning window. To apply optimal weights, the expressions are replaced by $w_{rn} = 3w_n \cos\phi_s$, $w_{zn} = 3w_n \sin\phi_s$ and $w_{pn} = w_n$.

For plane-wave beamforming consideration, an isospeed environment similar to Pekeris 150 m described in Chapter IV was assumed, i.e. depth 150 m, isospeed sound profile of 1500 m/s and bottom speed of 1600 m/s.

2. Results

To test the processor algorithm for beamforming, analytically defined signals incident on the array at 15°, and then at -20° and 15°, were computed. After confirmation of the code, the artificial plane waves were then replaced by the shallow water, simulated data from MMPE. The array simulated in Beamforming Techniques was different from that for MFP Techniques. Instead of 16 elements within a depth of 5 to 145 m (used for MFP processing), 256 elements were simulated in order to ensure the distance between elements was less than $\lambda/2$ (0.75 m) at 1000 Hz. This is required to prevent aliasing.

The results from the three sets of matched-field processing are shown together in each of the figures below and compared.

a) Beamforming Techniques Using Incoming Plane Wave at 15º

Figures 1 and 2 display the results of Beamforming Techniques processing of a simulated incoming plane-wave at 15º. Figure 2 provides a magnified representation near the incoming angle in order to emphasize the difference in gain between results derived from pressure only (blue curve), equal weight (green curve) and optimal weights (red curve) of AVS data (pressure, horizontal and vertical components of particle velocity). From Fig. 2, it is observed that the beamformer power at angle 15º (peak of the graph) for optimal weights of AVS data is approximately -95 dB, while that of pressure only is -101 dB, showing a difference of 6 dB. It is also observed that the gain of the equal weight AVS data exceeds that of pressure only data by about 5 dB at the same angle, consistent with the theoretical expectation of 4.8 dB [5].

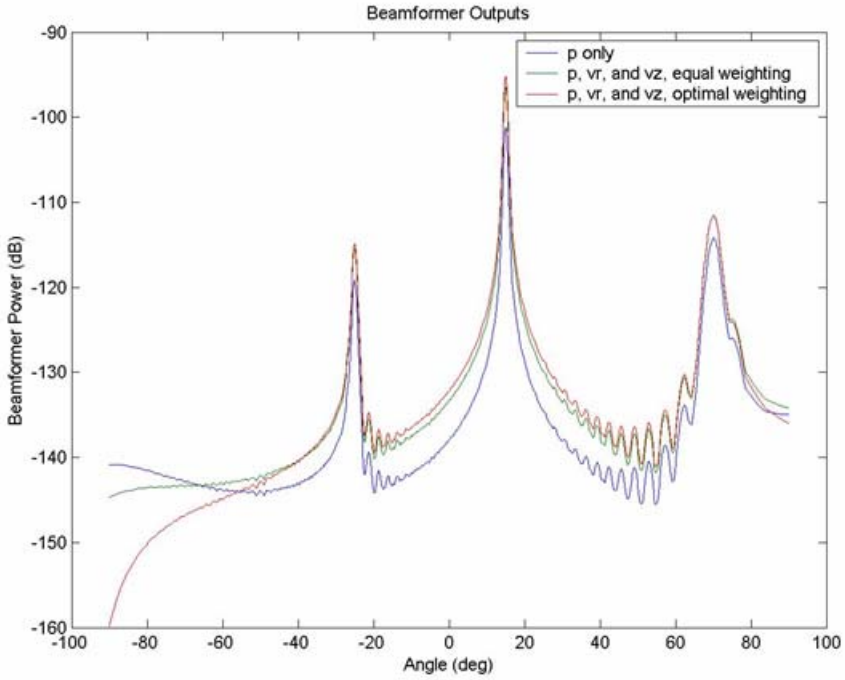

Figure 1. Result of three Beamforming Techniques processing using incoming plane-wave at 15°

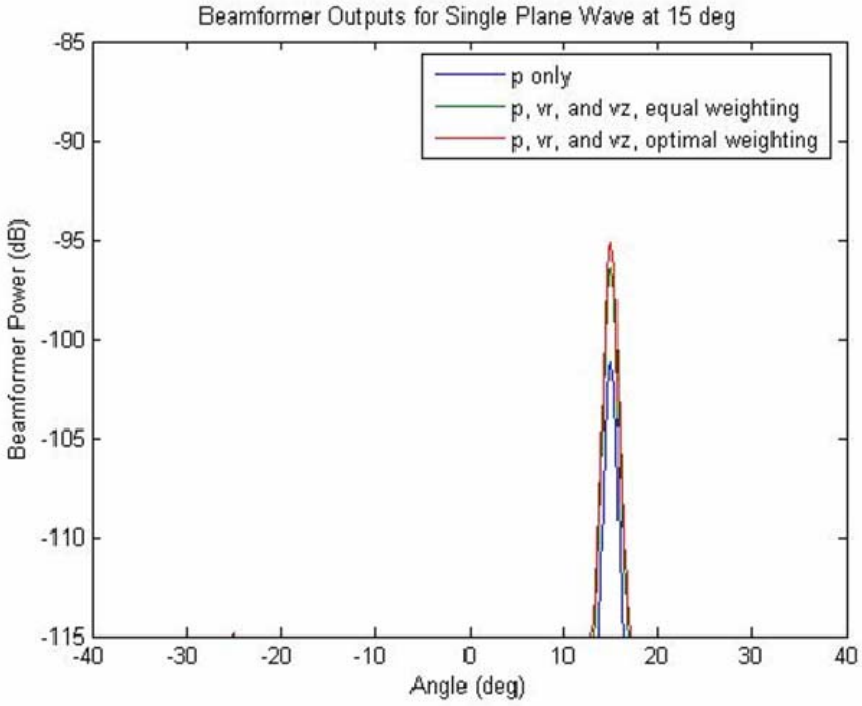

Figure 2. Zoomed in result of three Beamforming Techniques processing using incoming plane-wave at 15°

b) Beamforming Techniques Using Incoming Plane Waves at -20º and 15º

Likewise, Figs. 3 and 4 are the same plots that were the results of Beamforming Techniques processing applied to simulated incoming plane-waves at -20º and 15º. As before, Fig. 4 provides a magnified representation near the incoming angles in order to emphasize the difference in gain between results derived from pressure only (blue curve), equal weight (green curve) and optimal weights (red curve) of AVS data. From Fig. 4, it is observed that the beamformer power at angles -20º and 15º (both peaks) for optimal weights of AVS data were both approximately -95 dB, while that of pressure only were both -101 dB, showing again the difference of 6 dB. It is also observed that the gain of the equal weight AVS data exceeds that of pressure only data by about 5 dB at the same angles, as before.

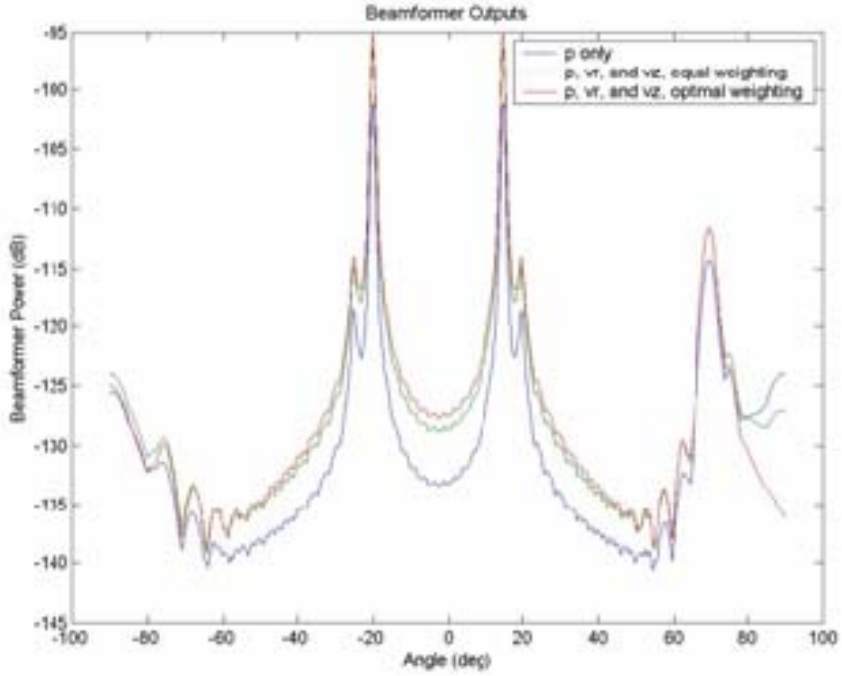

Figure 3. Result of three Beamforming Techniques processing using two incoming plane-waves at 15° and -20°

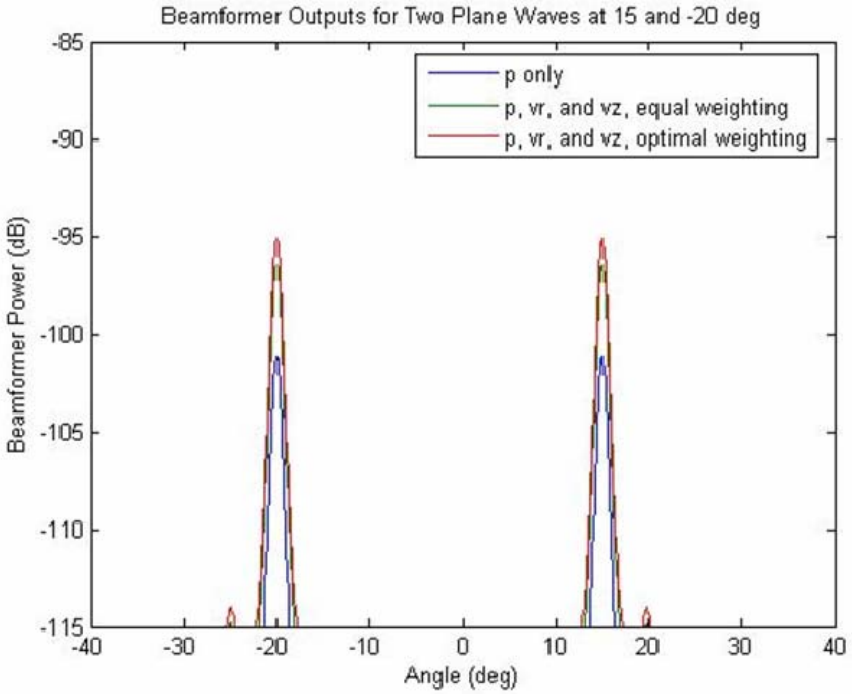

Figure 4. Zoomed in result of three Beamforming Techniques processing using two incoming plane-waves at 15° and -20°

c) Beamforming Techniques Using MMPE Simulated Signal

Figures 5 and 6 are the same types of plots for the Beamforming Techniques processing using MMPE to simulate the incoming signal. Figure 6 provides a magnified representation over the range of angles presenting the highest peaks of the curve in order to emphasize the difference in gain between results derived from pressure only (blue curve), equal weight (green curve) and optimal weights of AVS data (red curve). From Fig. 6, it can be observed that the difference in gain at the numerous peaks is approximately 6 dB between optimal weights of AVS data and pressure only data, while the difference between equal weight of AVS data and pressure only data is about 5 dB.

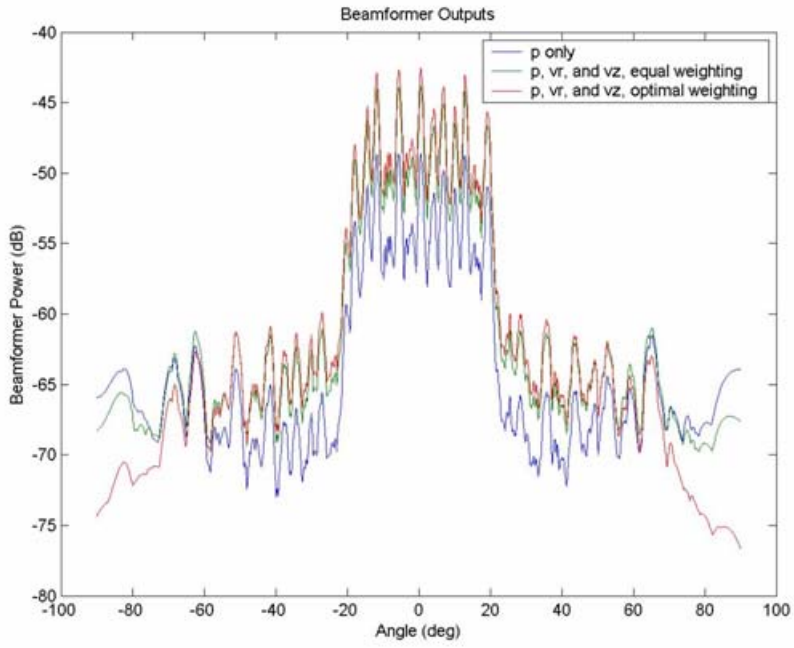

Figure 5. Result of three Beamforming Techniques processing using simulated data from MMPE

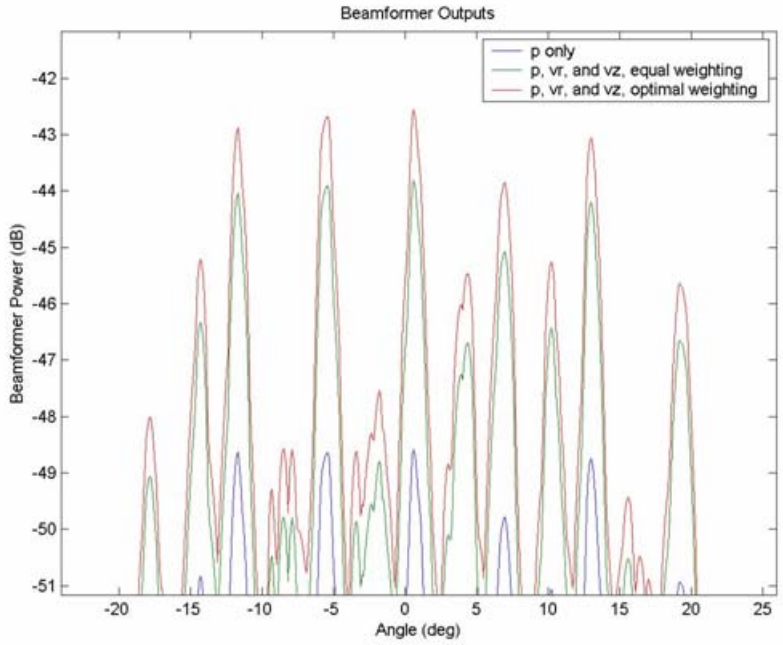

Figure 6. Zoomed in result of three Beamforming Techniques processing using simulated data from MMPE

3. Conclusion from Beamforming Techniques

It can be confirmed from all the Figs. 1 to 6 above that the AVS array (with p, v_r and v_z components) outperforms the simple hydrophone array. It can also be observed that the maximum gain of the AVS array over the hydrophone array using linear, plane-wave beamforming was 6 dB, as predicted for optimal weighting. These observations confirmed that the processor algorithm had performed according to theory provided in [5] and was working to specifications. This processor can now be applied to the MFP Techniques.

C. MATCHED-FIELD PROCESSING TECHNIQUES

Similar to the Beamforming Techniques, there were also three versions of MFP Techniques intended to show the difference in performance between AVS and hydrophone arrays. The three versions were varied by their weightings as follow:

- using pressure only;
- using equal weights for pressure (p), horizontal (v_r) and vertical (v_z) components of particle velocity;
- using component (p, v_r and v_z) weights that equalize the mean square component signal.

1. Theory

One difference between MFP and Beamforming Techniques was that MFP employed MMPE simulated data for both measured data and replica. In plane-wave beamforming, the replica is an analytically defined plane-wave. In standard MFP techniques, the replica is generated by a numerical model, usually employed in a reciprocal fashion.

For example, in this study, the “measured data” is recorded on 16 elements of a vertical array at varying range, as predicted by MMPE using a point source at range $r = 0$. Regardless of how the measured data is generated, the replica data is then created by running the model in a reciprocal fashion using a point source at each receiver element

location and storing the solution at every computational grid point within the search space. By reciprocity, the solution at each grid point is equivalent to what would be received at the array element location from a point source at that grid point. The calculation of these reciprocal fields from all 16 receiver element locations can then be combined into a 16 element replica for each grid point in the search space. Naturally, the ambiguity levels obtained using model-model correlations should be expected to be higher than that from model-measurement correlations.

No Hanning window was applied for the MFP Techniques, which also assumed 16 elements instead of 256 in the array ranging from 5 to 145 m depth. The simulated data was obtained by setting a source at 35 m and varying distances of approximately 5, 10 and 15 km away. The replica field was then created by running the MMPE model using the known 16 sensor positions as reciprocal sources and computing the field at every point in space (on the computational grid). The challenge in the process of MFP techniques was the correct application of weightings to each component. Unlike in Beamforming Techniques, the replicas of each component cannot be assumed equal. It was observed that the relative magnitude of components, e.g. between p and v_z , can vary up to a few orders of magnitude, hence the weightings may have a significant effect on the results, allowing smaller valued components to have a greater influence.

The algorithm for MFP techniques is given by

$$B = \left| \sum_{n=0}^{N-1} \left[w_n^{(1)} v_n^{(1)} \left(R_n^{(1)} \right)^* + w_n^{(2)} v_n^{(2)} \left(R_n^{(2)} \right)^* + w_n^{(3)} v_n^{(3)} \left(R_n^{(3)} \right)^* + w_{pn} v_{pn} \left(R_{pn} \right)^* \right] \right|^2 \qquad (3.5)$$

$$= \left| \sum_{n=0}^{N-1} \left[w_{rn} v_{rn} \left(R_{rn} \right)^* + w_{zn} v_{zn} \left(R_{zn} \right)^* + w_{pn} v_{pn} \left(R_{pn} \right)^* \right] \right|^2 ,$$

where $w_n^{(3)} v_n^{(3)} \left(R_n^{(3)} \right)^* = 0$, as this thesis assumed azimuthal symmetry. Equal weightings were realized by normalizing the signal of each component individually to ensure equal contributions. The component weights that equalize the mean square component signal are given by

$$\sum_{n=0}^{N-1} w_{rn} \left| v_{rn} \right|^2 = \sum_{n=0}^{N-1} w_{zn} \left| v_{zn} \right|^2 = \sum_{n=0}^{N-1} w_{pn} \left| v_{pn} \right|^2 \quad . \tag{3.6}$$

The results from MFP Techniques are shown in Chapter IV.

THIS PAGE INTENTIONALLY LEFT BLANK

IV. NUMERICAL RESULTS AND ANALYSIS

A. MODELING SETUP

Modeling was carried out using the MMPE program described in Chapter II. An underwater source was arbitrarily set at 35 meters depth and driven at 1000 Hz. Two different types of environments were used and each environment was varied with 2 different types of perturbations. The range of the source was varied at 5.49, 11.02 and 15.42 km. For convenience, these ranges will be referred to as 5, 10 and 15 km.

1. Environments

The 2 different environments used for modeling were termed the Pekeris 150 m and Mixed Layer 150 m. Their corresponding parameters are described below.

SOUND SPEED PROFILE AT RANGE = 0.00 km

DEPTH(m)	SOUND SPEED(m/s)
0.00	1500.00
150.00	1500.00

BOTTOM DEPTH

RANGE(km)	DEPTH(m)
0.00	150.00

BOTTOM PROPERTIES

RANGE(km)	VELOCITY(m/s)	GRADIENT(1/s)	DENSITY	LOSS(dB/km/Hz)	SHEAR(m/s)	SHEAR LOSS(dB/km/Hz)
0.00	1600.00	0.00	1.20	0.1000	0.00	0.0000

FFT size, nz = 16384 and depth mesh, dz = 9.7656250E-02 m.
Range step, dr = 1.5000000E-03 km.
Outputting 1000 points from 0.0000000E+00 km to 16.00000 km in range.
Outputting 911 points from 4.8828125E-02 m to 799.8535 m in depth.
Outputting 1 radials separated by 0.0000000E+00 deg.

Table 1. Parameters of Pekeris 150 meters depth

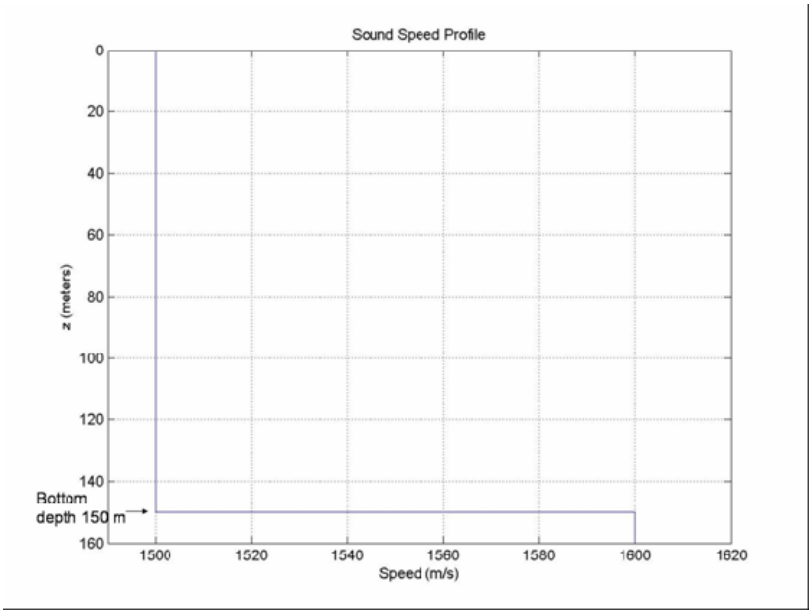

Figure 7. Sound speed profile of Pekeris 150 meters depth

SOUND SPEED PROFILE AT RANGE = 0.00 km

DEPTH(m)	SOUND SPEED(m/s)
0.00	1524.00
60.00	1525.00
150.00	1494.00
800.00	1270.11

BOTTOM DEPTH

RANGE(km)	DEPTH(m)
0.00	150.00

BOTTOM PROPERTIES

RANGE(km)	VELOCITY(m/s)	GRADIENT(1/s)	DENSITY	LOSS(dB/km/Hz)	SHEAR(m/s)	SHEAR LOSS(dB/km/Hz)
0.00	1600.00	0.00	1.20	0.1000	0.00	0.0000

FFT size, nz = 16384 and depth mesh, dz = 9.7656250E-02 m.
Range step, dr = 1.5000000E-03 km.
Outputting 500 points from 0.0000000E+00 km to 16.00000 km in range.
Outputting 911 points from 4.8828125E-02 m to 799.8535 m in depth.
Outputting 1 radials separated by 0.0000000E+00 deg.

Table 2. Parameters of Mixed Layer 150 meters depth[1]

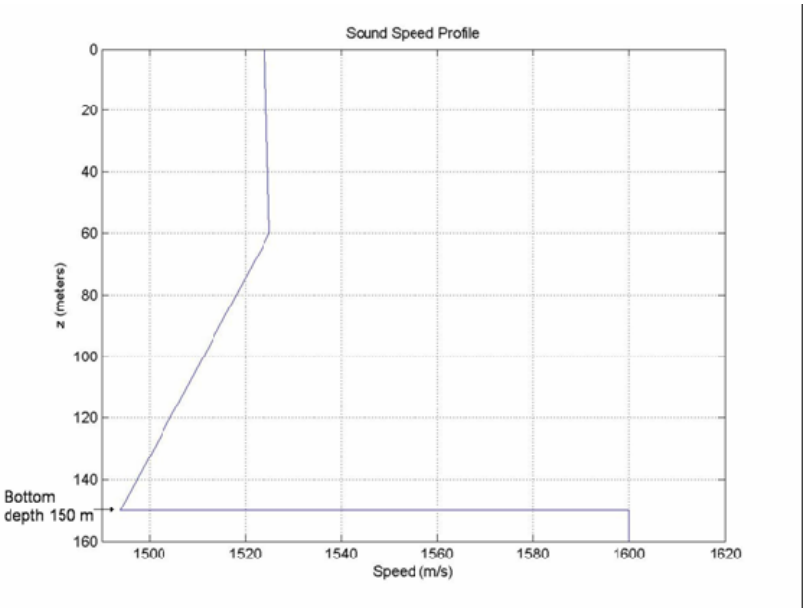

Figure 8. Sound speed profile of Mixed Layer 150 meters depth

[1] Taken from Pg. 148 of [13].

2. Different Perturbations

The 2 different types of perturbations[2] integrated in the modeling were

- No perturbation (P1) and
- Interface roughness (P2).

No perturbation (P1) is quite self-explanatory, it does not take into account any kind of perturbation. Though unrealistic, this condition provides a baseline for reference in this thesis.

Based on [14], interface roughness (P2) incorporates the effects of a rough water/bottom interface by creating realizations of bathymetric fluctuations based on an isotropic, 1-D, empirical spectrum. The interface roughness (P2) condition allowed the MFP Techniques to be tested in a more challenging environment in order to better evaluate the difference in performance between hydrophone and AVS arrays. The results from this environmental condition also aid in verifying the techniques of this thesis.

3. Modeling Procedure

The MMPE program was first run using the source set at 35 meters depth with each of the given set of parameters. The output was a matrix of vectors representing the acoustic field at all depth and range indices. The acoustic field information consists of the pressure (p) field information, horizontal component (v_r) of the particle velocity information and vertical component (v_z) of the particle velocity information. At each range and depth index, the information of each component (p, v_r and v_z) is represented by a corresponding complex number representing its magnitude and phase.

An array was then represented by 16 sensors at depths spanning between 5 to 145 meters. It is important to note that the reciprocal sensor runs were carried out only with the No Perturbation (P1) option. This was deliberately done in order to predict the expected replica field in the absence of perturbations. The perturbations were only used to generate the simulated data to represent more realistic signal fluctuations.

[2] These perturbations were created and integrated into MMPE by Smith.

Using the principle of reciprocity, the 16 sets of sensor information was correlated with the source information (as described in Chapter III) in order to localize the correct source range and depth. An Ambiguity Surface (AMS) is plotted through MATLAB to illustrate the correlation and localization. The Ambiguity Surface was used to compare the difference in performances between hydrophone array and AVS array.

B. RESULTS AND ANALYSIS

The results were examined for the two applied environments, Pekeris 150 m and Mixed Layer 150 m. The sources were located at 35 m depth, at ranges of 5.49 km, 11.02 km, or 15.42 km for the 5 km, 10 km, and 15 km runs, respectively.

1. Results for Pekeris 150 m Environment

The results from the Pekeris 150 m environment were divided into different ranges of 5 km, 10 km and 15 km. The three AMS plots representing the three different weightings (i.e. pressure only, equal and equalized weightings of AVS data) are followed by two more plots of the same conditions illustrating the variation of the normalized AMS values near the actual source location across depth and range respectively. Results for no perturbation (P1) are presented before interface roughness (P2).

a) Pekeris 150 m, 5 km, 1000 Hz, no Perturbation

Comparing the AMS plots (Figs. 9-11) computed from the respective weightings of data, it is observed that all three plots have the source clearly localized at the correct position, though the equal weighting AMS plot signal appears the weakest. It should be pointed out that the higher the AMS level, the more confidence we have that the source is located at a given position. So a high AMS level at the correct source level indicates good processor performance. However, high levels at other locations indicate poor processor performance. Comparing the variability of the ambiguity surfaces in Figs. 9-11, it is obvious that the equalized weight AMS plot has the highest variability which corresponds to the most difficulty in source localization. This is followed by the pressure only AMS plot. Figure 12 provides the normalized AMS values (or correlation values) at

range 5.49 km (known source range) against depth while Fig. 13 provides the normalized AMS (or correlation) values at depth 35 m (known source depth) against range. These two plots reinforce the observations made from Figs. 10-12.

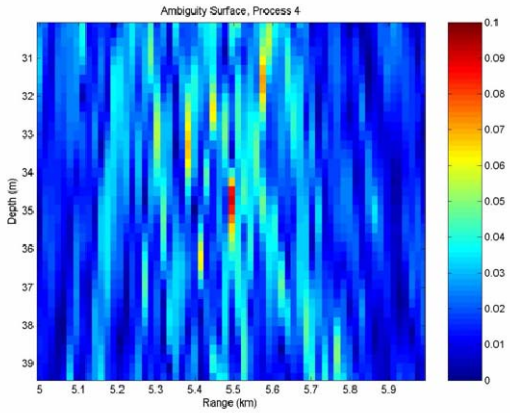

Figure 9. AMS plot for pressure only at 5 km, 1000 Hz, with no perturbation

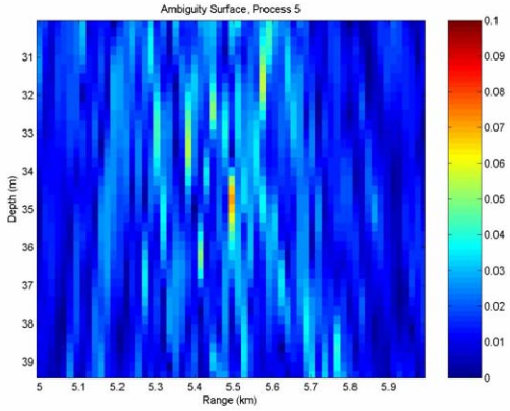

Figure 10. AMS plot for equal weighting of p, v_r and v_z at 5 km, 1000 Hz, with no perturbation

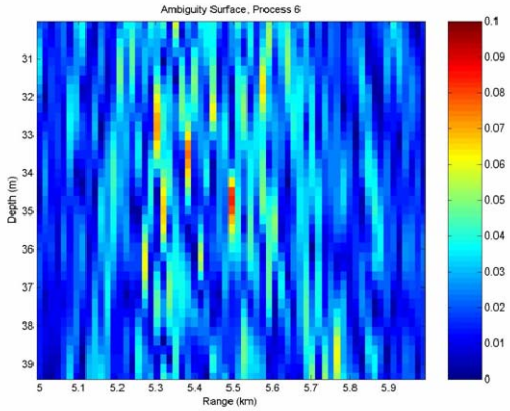

Figure 11. AMS plot for equalized weightings of p, v_r and v_z at 5 km, 1000 Hz, with no perturbation

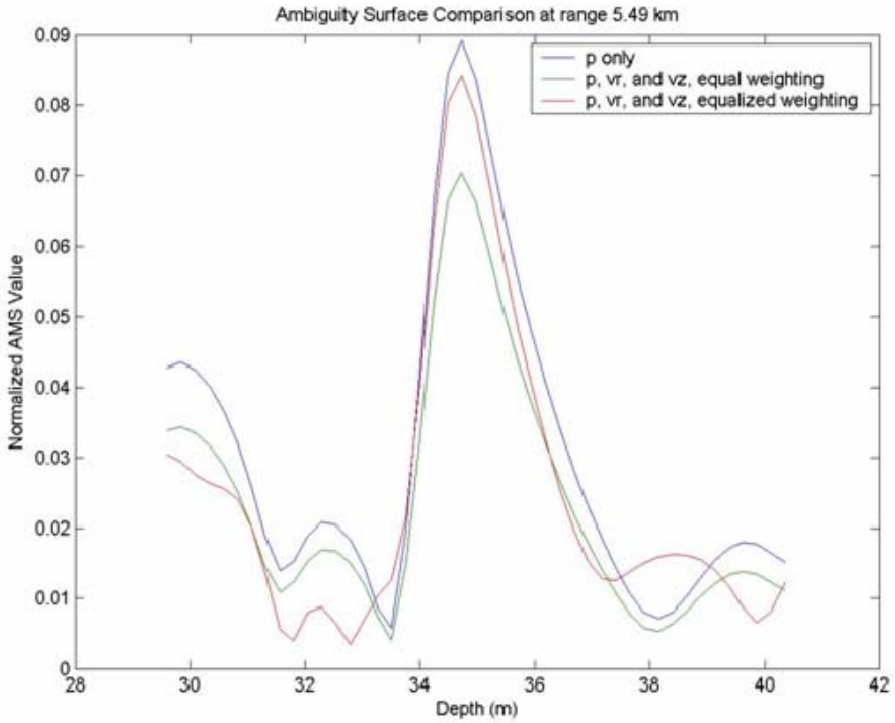

Figure 12. Normalized AMS value vs. depth plot at range 5.49 km

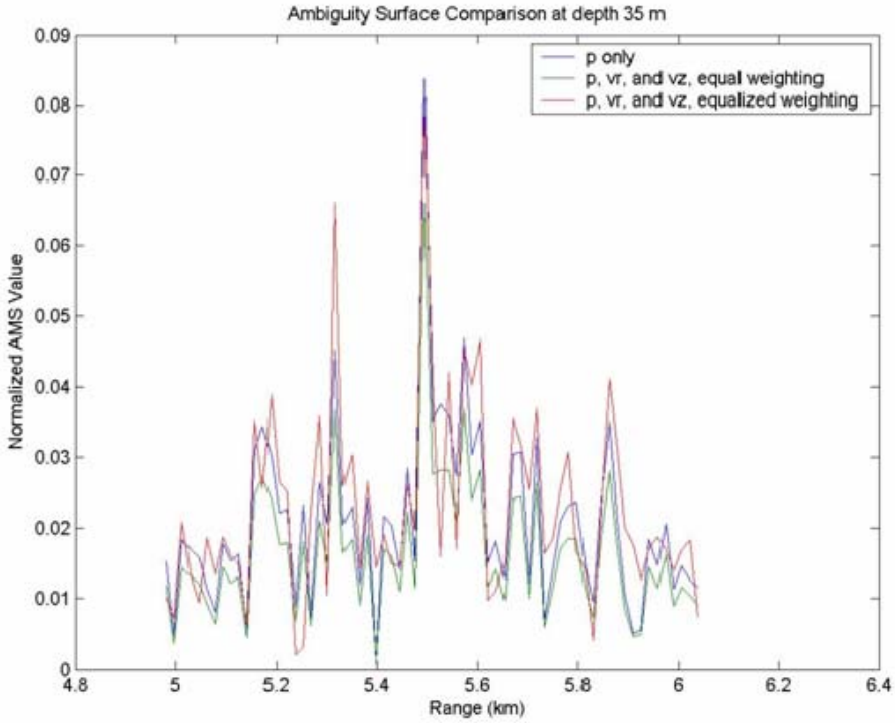

Figure 13. Normalized AMS value vs. range plot at depth 35 m

b) Pekeris 150 m, 10 km, 1000 Hz, no Perturbation

Comparing the AMS plots (Figs. 14-16) computed from the respective weightings of data, it is observed that all three plots have the source clearly localized at the correct position without any signal looking particularly stronger or weaker. Comparing the variability of the ambiguity surfaces, it is clear that the equalized weight AMS plot had the highest level of variability while that for the other two plots were fairly similar. Figure 17 provides the normalized AMS values at range 11.02 km (known source range) against depth while Fig. 13 provides the normalized AMS values at depth 35 m (known source depth) against range. Comparing the three curves in Fig. 17 at 35 m depth, it is shown that the highest normalized AMS value is achieved by the equalized weighting AVS data, followed by the pressure only data and the equal weighting AVS data. As observed in Fig. 16, Fig. 18 reinforces that the equalized weighting AVS data has the highest level of variability.

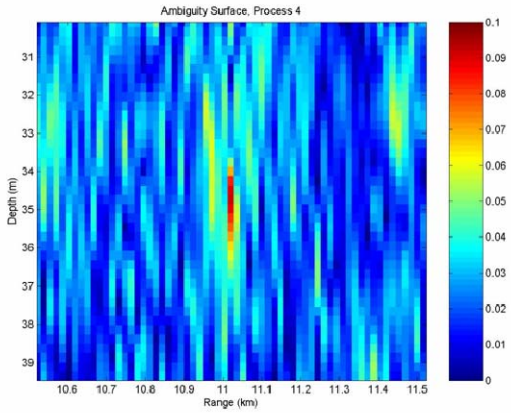

Figure 14. AMS plot for pressure only at 10 km, 1000 Hz, with no perturbation

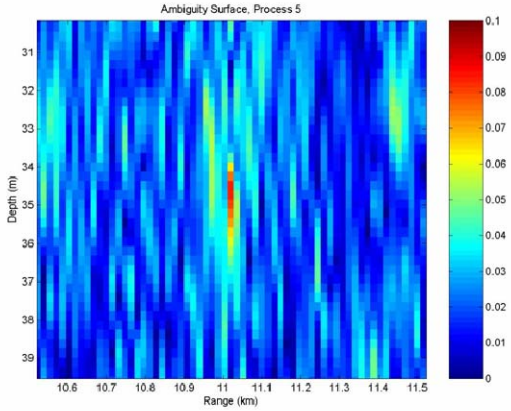

Figure 15. AMS plot for equal weighting of p, v_r and v_z at 10 km, 1000 Hz, with no perturbation

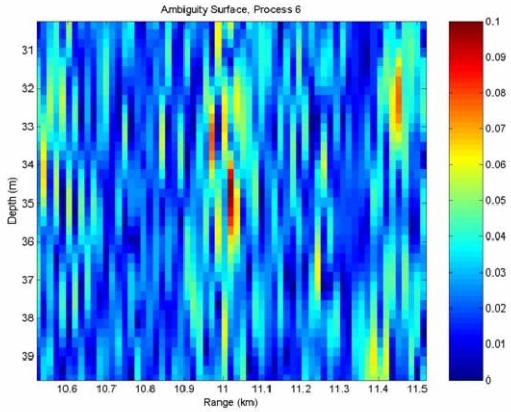

Figure 16. AMS plot for equalized weightings of p, v_r and v_z at 10 km, 1000 Hz, with no perturbation

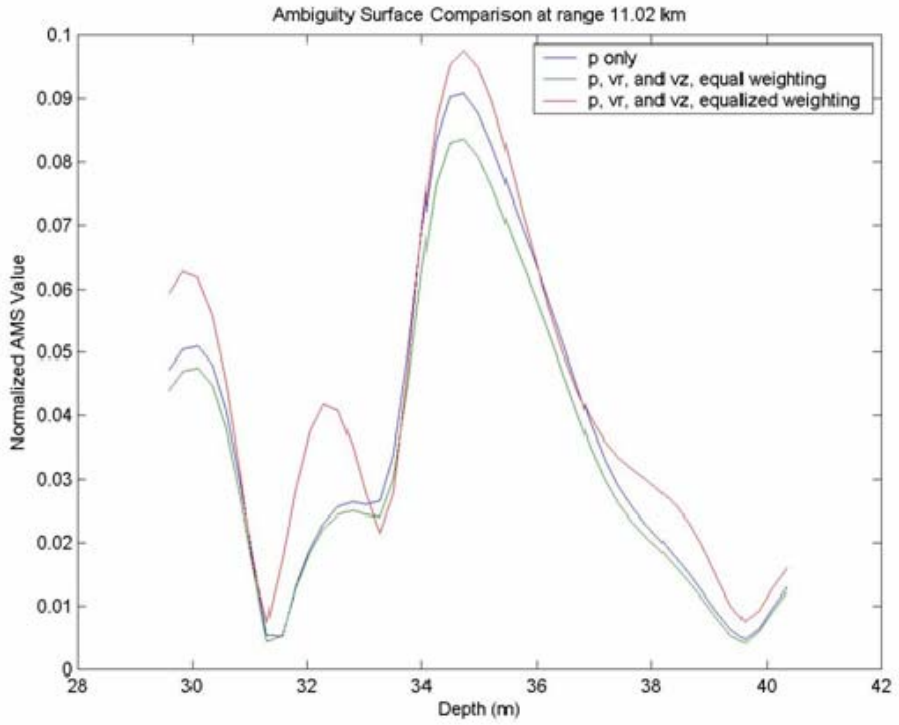

Figure 17. Normalized AMS value vs. depth plot at range 11.02 km

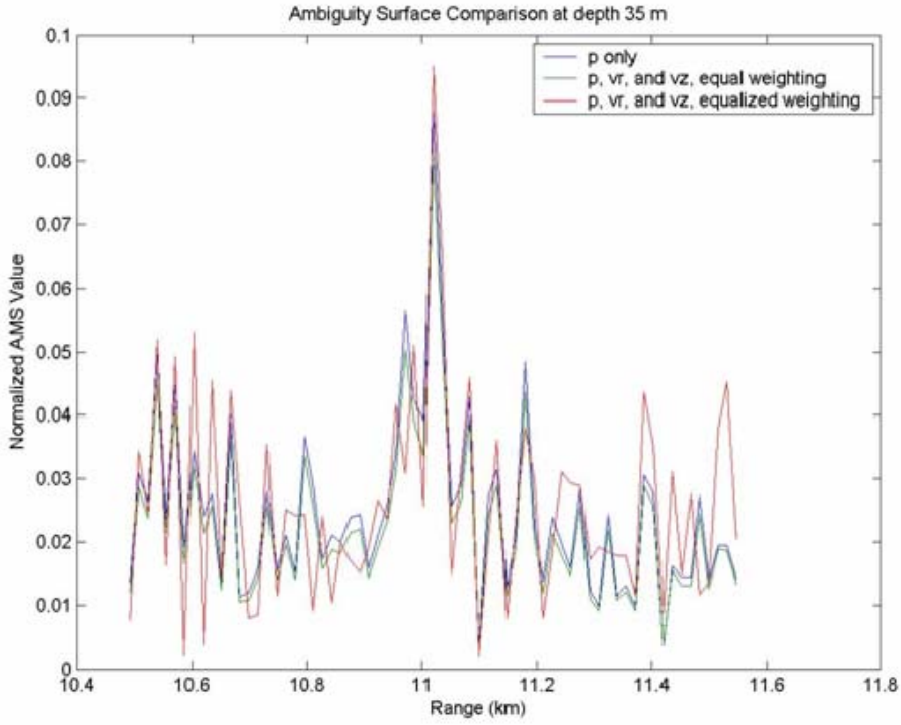

Figure 18. Normalized AMS value vs. range plot at depth 35 m

c) Pekeris 150 m, 15 km, 1000 Hz, no Perturbation

Comparing the AMS plots (Figs. 19-21) computed from the respective weightings of data, it is observed that all three plots have the source clearly localized at the correct position without any signal looking particularly stronger or weaker. The variability of the ambiguity surfaces is higher than all previous plots, though it is obvious that the equalized weight AMS plot still has the highest level followed by the pressure only AMS plot. Figure 22 provides the normalized AMS values at range 15.42 km (known source range) against depth and Fig. 23 provides the normalized AMS values at depth 35 m (known source depth) against range. These two plots reinforce the observations made from Figs. 19-21 that the normalized AMS values in both plots are relatively similar for all three types of data.

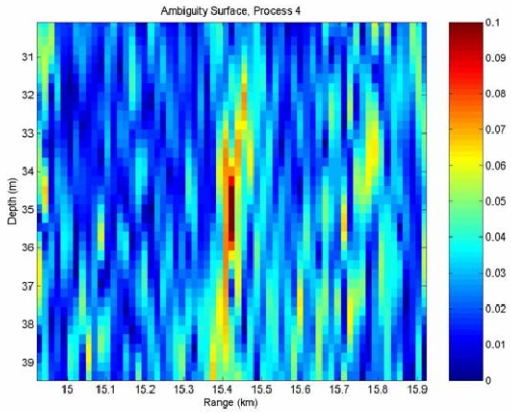

Figure 19. AMS plot for pressure only at 15 km, 1000 Hz, with no perturbation

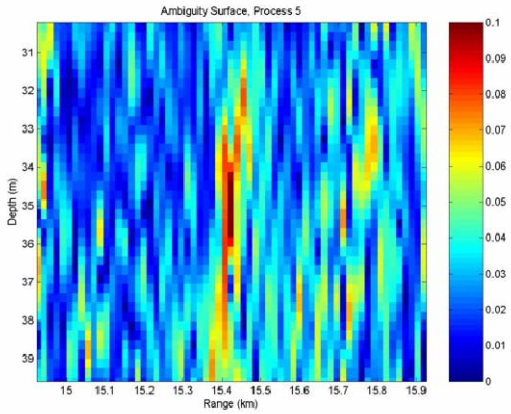

Figure 20. AMS plot for equal weighting of p, v_r and v_z at 15 km, 1000 Hz, with no perturbation

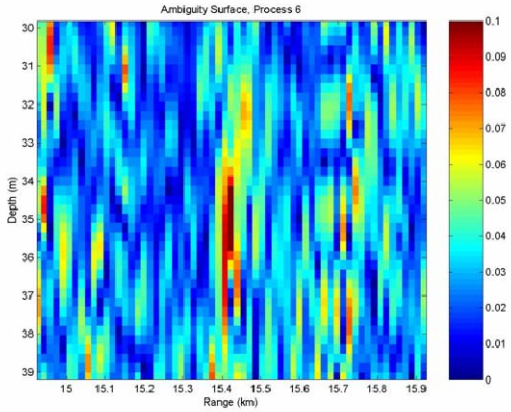

Figure 21. AMS plot for equalized weightings of p, v_r and v_z at 15 km, 1000 Hz, with no perturbation

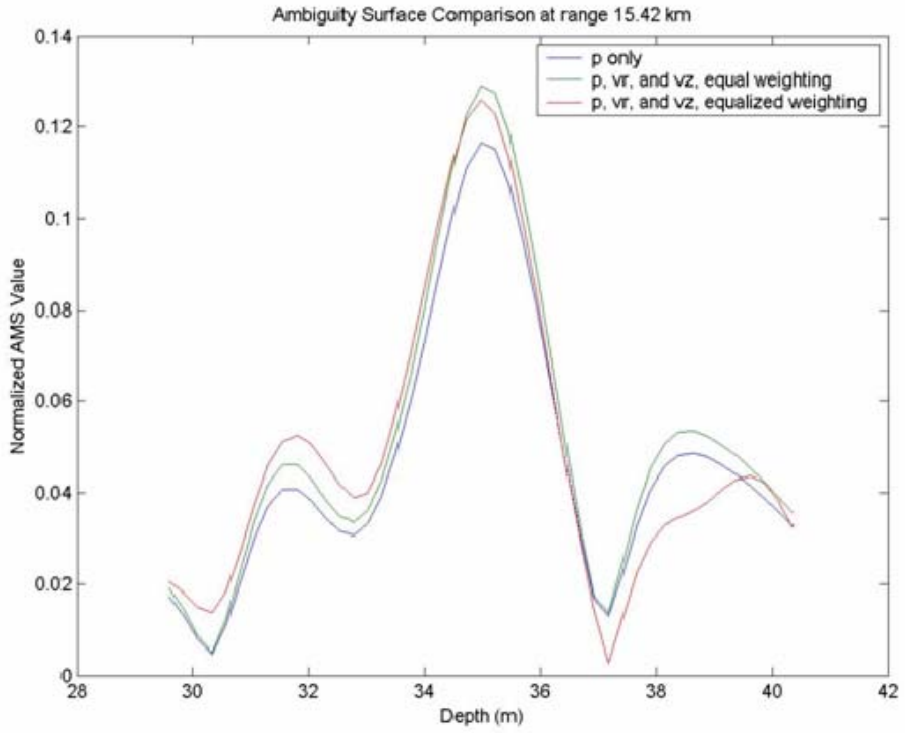

Figure 22. Normalized AMS value vs. depth plot at range 15.42 km

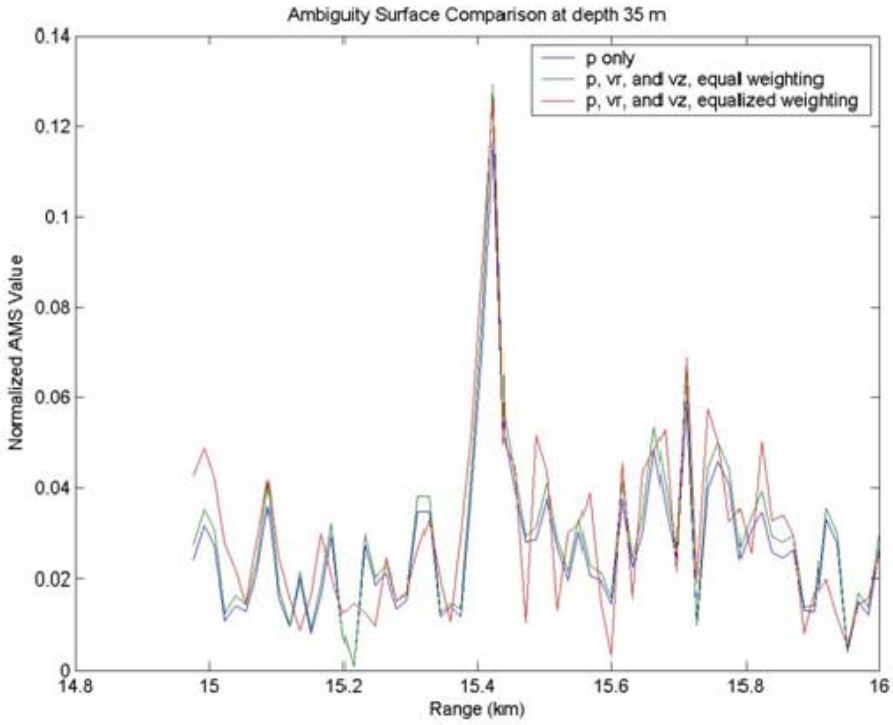

Figure 23. Normalized AMS value vs. range plot at depth 35 m

d) Pekeris 150 m, 5 km, 1000 Hz, Interface Roughness

Comparing the AMS plots (Figs. 24-26) computed from the respective weightings of data, it is observed in all three plots that the perturbed interface greatly reduces our ability to localize the source. The variability of the ambiguity surfaces is low and fairly similar for all three plots. Figure 27 provides the normalized AMS values at range 5.49 km (known source range) against depth while Fig. 28 provides the normalized AMS values at depth 35 m (known source depth) against range. In Fig. 27, all three curves display a peak at 34 m, though this was not discernible in Figs. 24-26. Figure 28 also shows a peak at about 5.49 km for all three curves though these were not much higher than the surrounding noise, reinforcing the observations from Figs. 24-26.

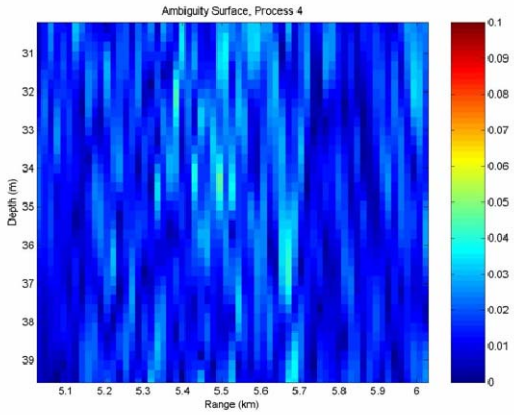

Figure 24. AMS plot for pressure only at 5 km, 1000 Hz, with interface roughness

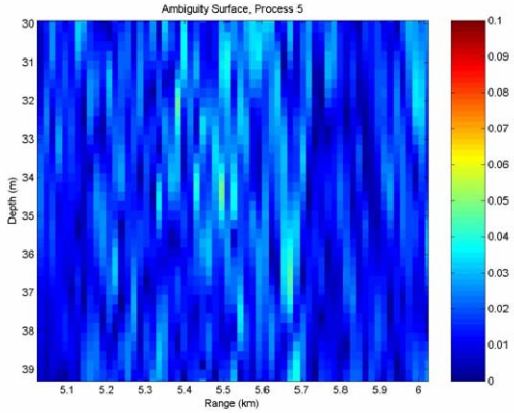

Figure 25. AMS plot for equal weighting of p, v_r and v_z at 5 km, 1000 Hz, with interface roughness

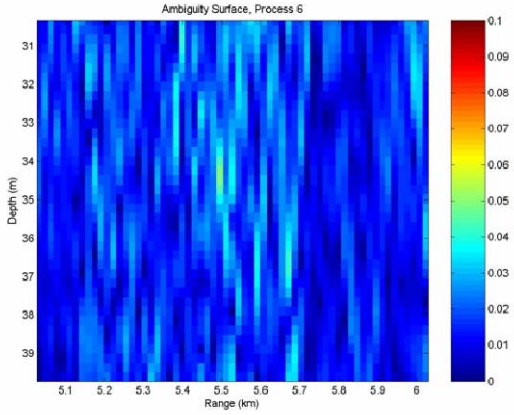

Figure 26. AMS plot for equalized weightings of p, v_r and v_z at 5 km, 1000 Hz, with interface roughness

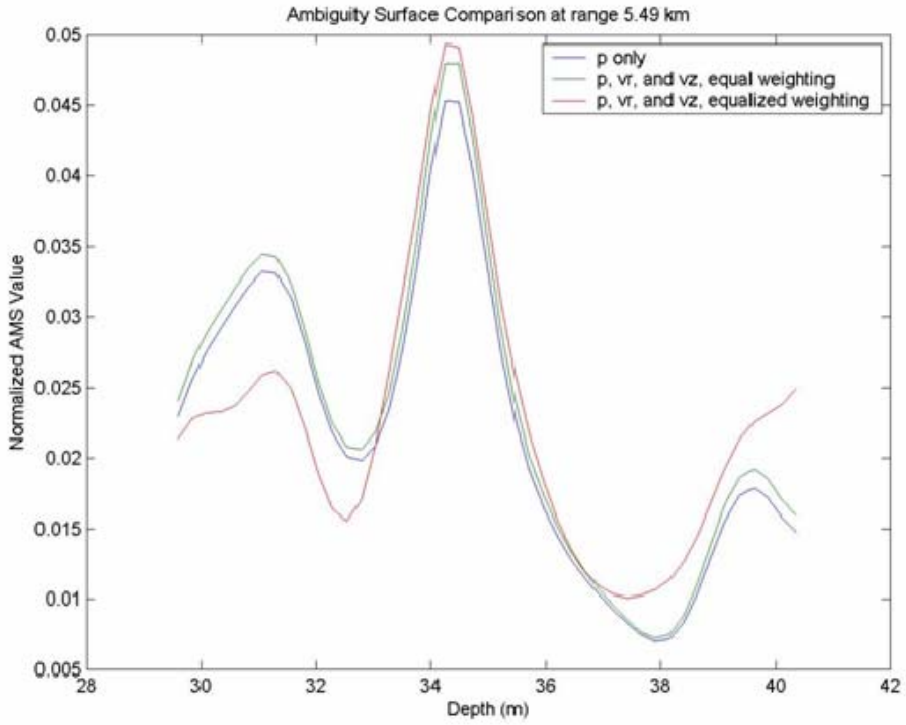

Figure 27. Normalized AMS value vs. depth plot at range 5.49 km

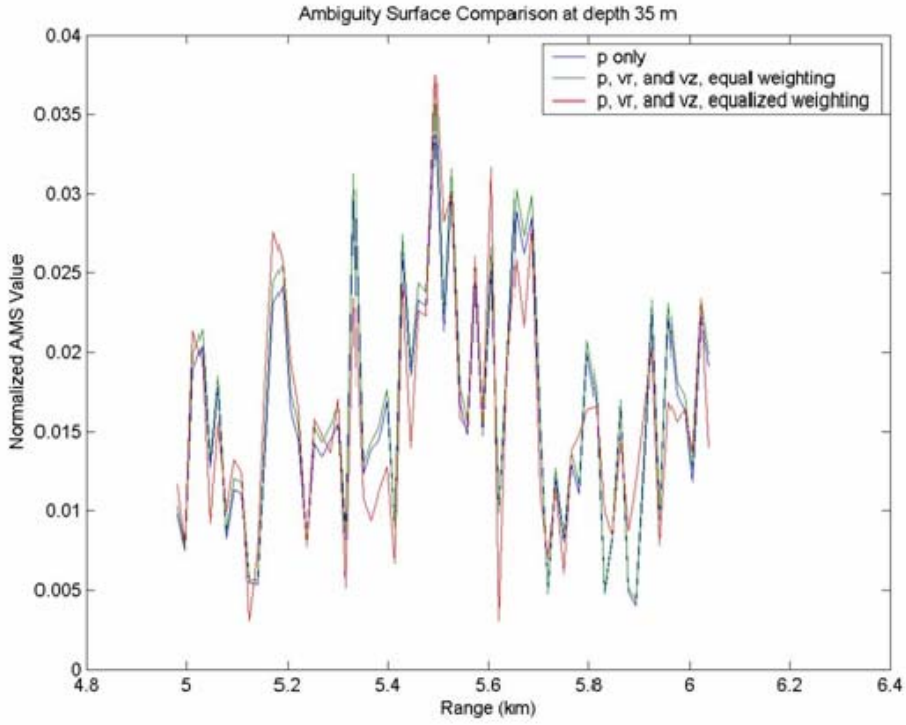

Figure 28. Normalized AMS value vs. range plot at depth 35 m

e) Pekeris 150 m, 10 km, 1000 Hz, Interface Roughness

Comparing the AMS plots (Figs. 29-31) computed from the respective weightings of data, it is observed that all three plots have significant difficulty in localizing the source. The variability of the ambiguity surfaces is low and fairly similar for all three plots. Figure 32 provides the normalized AMS values at range 11.02 km (known source range) against depth while Fig. 33 provides the normalized AMS values at depth 35 m (known source depth) against range. In Figs. 32-33, the highest peaks are not distinct for any of the three curves, reinforcing the observations from Figs. 29-31.

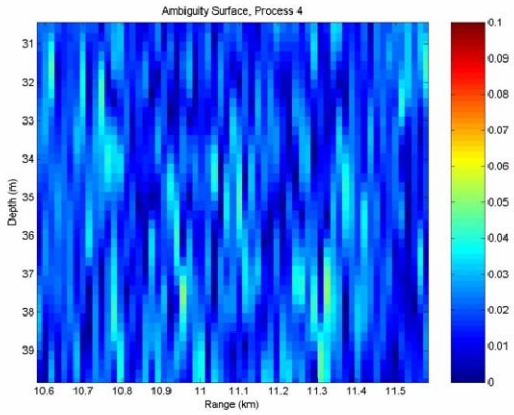

Figure 29. AMS plot for pressure only at 10 km, 1000 Hz, with interface roughness

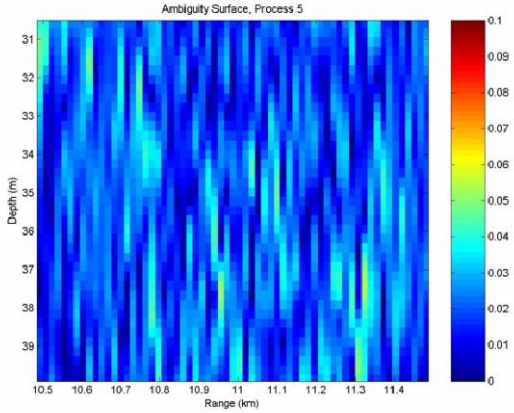

Figure 30. AMS plot for equal weighting of p, v_r and v_z at 10 km, 1000 Hz, with interface roughness

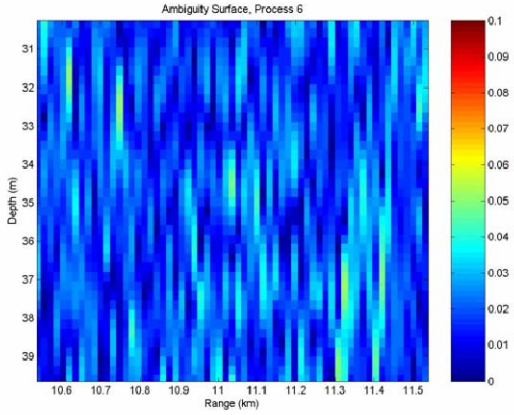

Figure 31. AMS plot for equalized weightings of p, v_r and v_z at 10 km, 1000 Hz, with interface roughness

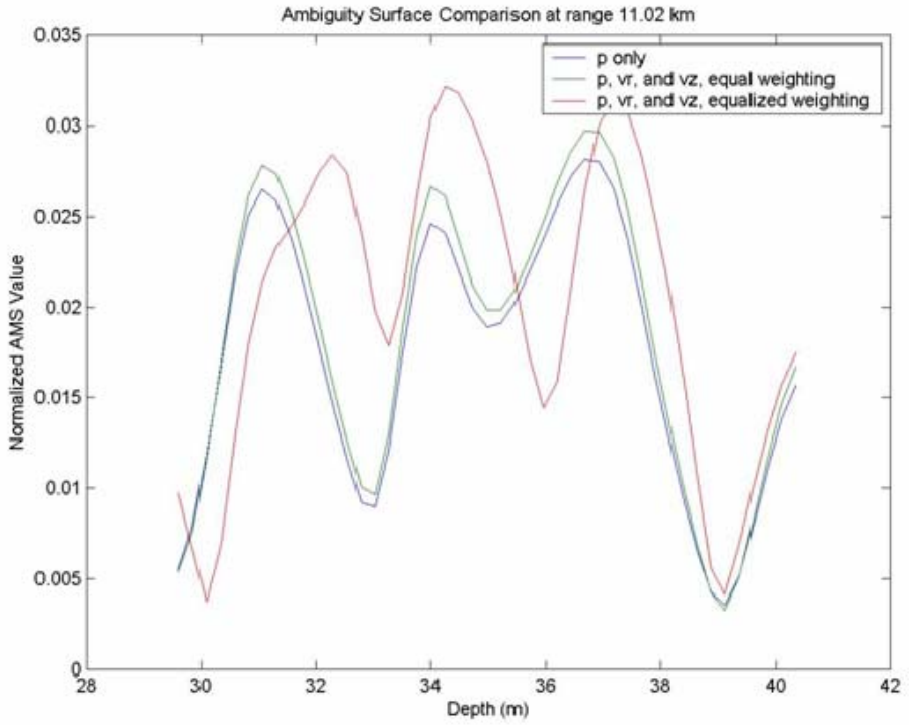

Figure 32. Normalized AMS value vs. depth plot at range 11.02 km

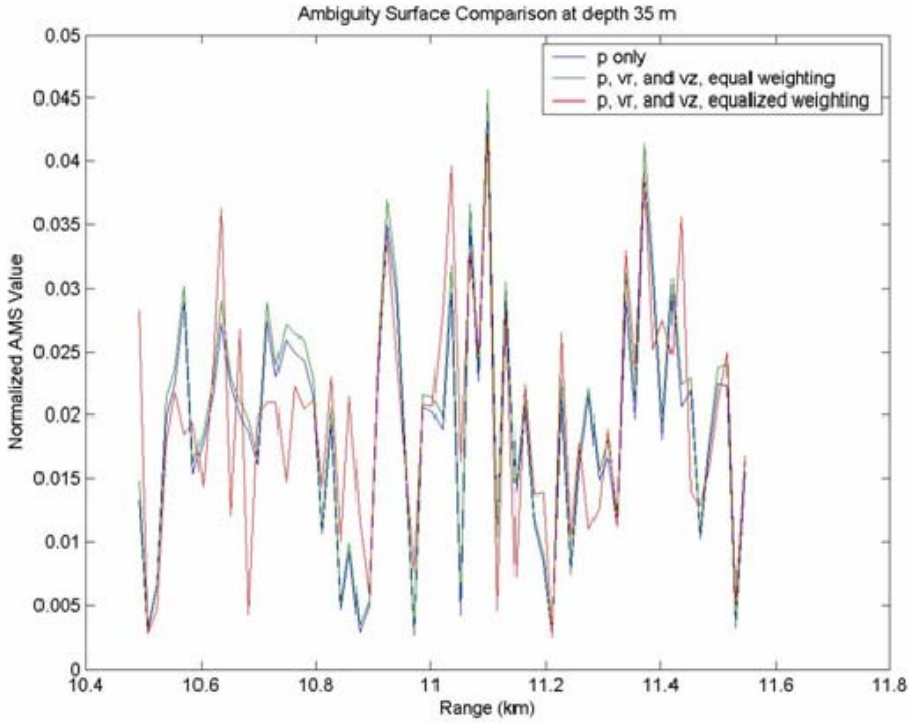

Figure 33. Normalized AMS value vs. range plot at depth 35 m

f) Pekeris 150 m, 15 km, 1000 Hz, Interface Roughness

Comparing the AMS plots (Figs. 34-36) computed from the respective weightings of data, it is observed that all three plots appear to localize a source at approximately 15.12 km range, 34 m depth, which is not the known source position. The variability of the ambiguity surfaces is high for all three plots. The equalized weighting AVS data has the highest variability followed by the pressure only data. Figure 37 provides the normalized AMS values at range 15.42 km (known source range) against depth while Fig. 38 provides the normalized AMS values at depth 35 m (known source depth) against range. There appears to be a peak at 38 m in Fig. 37 and 15.12 km in Fig. 38. While the peak in Fig. 38 seems to conform to the observations from Figs. 34-36, the peak in Fig. 37 is not apparent in other plots.

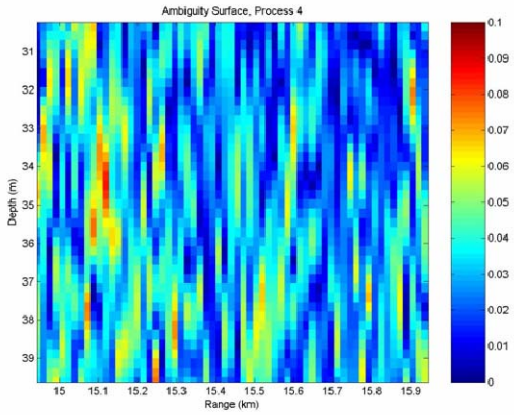

Figure 34. AMS plot for pressure only at 15 km, 1000 Hz, with interface roughness

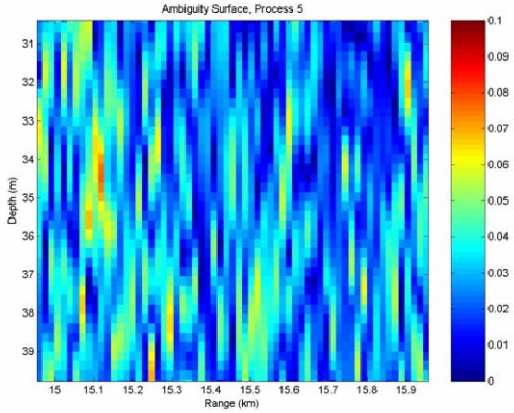

Figure 35. AMS plot for equal weighting of p, v_r and v_z at 15 km, 1000 Hz, with interface roughness

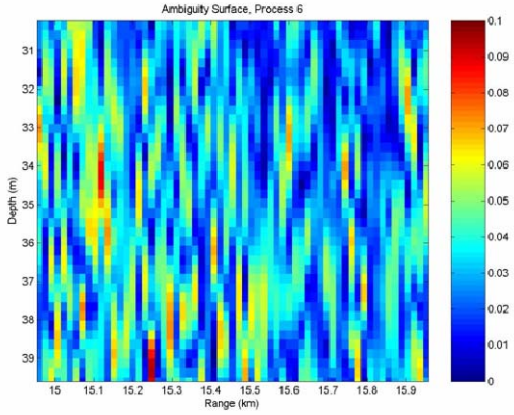

Figure 36. AMS plot for equalized weightings of p, v_r and v_z at 15 km, 1000 Hz, with interface roughness

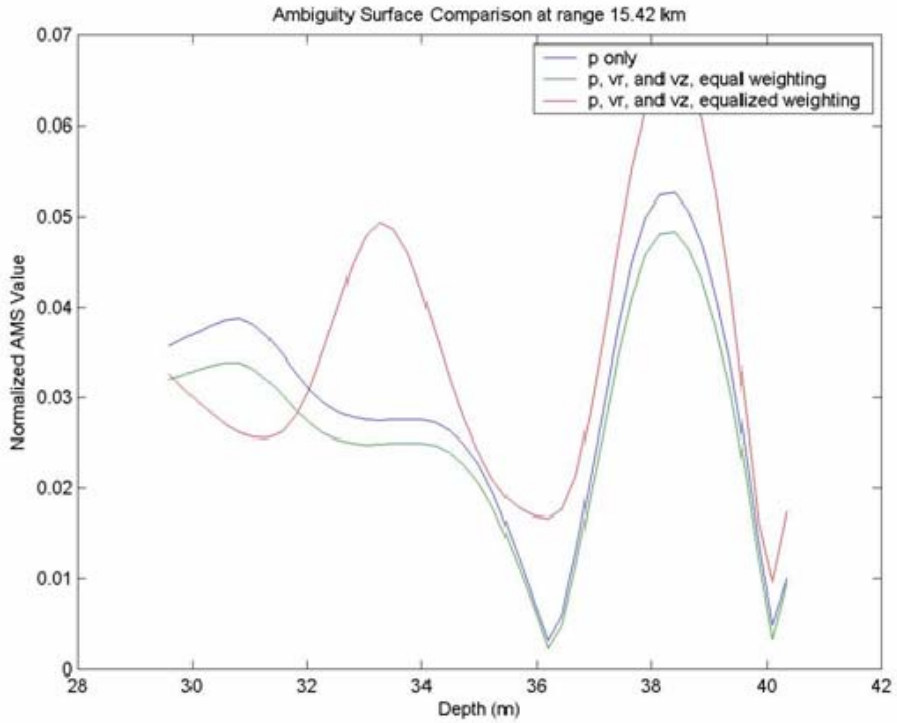

Figure 37. Normalized AMS value vs. depth plot at range 15.42 km

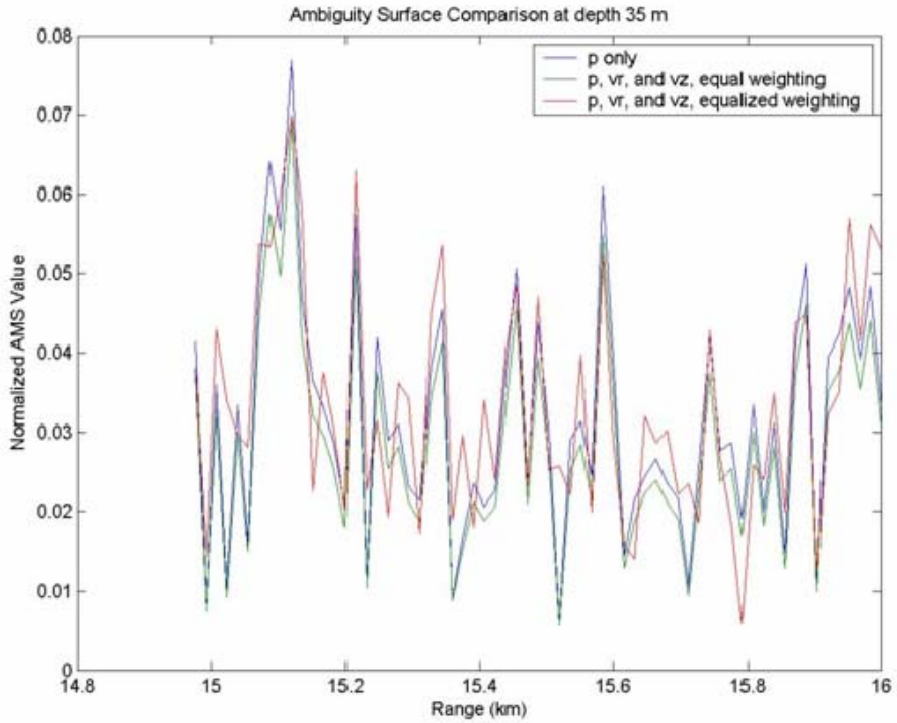

Figure 38. Normalized AMS value vs. range plot at depth 35 m

2. Results from Mixed Layer 150 m Environment

The results from applying the Mixed Layer 150 m environment were divided into different ranges of 5 km, 10 km and 15 km. The results for no perturbation (P1) are presented before interface roughness (P2).

a) Mixed Layer 150 m, 5 km, 1000 Hz, no perturbation

Comparing the AMS plots (Figs. 39-41) computed from the respective weightings of data, it is observed that all three plots have the source fairly well localized at the correct position, without any apparent difference in strength. Comparing the variability of the ambiguity surfaces, it is obvious that the equalized weight AMS plot has the highest level, while that of the other two plots are similar. Figure 42 provides the normalized AMS values at range 5.49 km (known source range) against depth while Fig. 43 provides the normalized AMS values at depth 35 m (known source depth) against range. These two plots reinforce the observations made from Figs. 39-41.

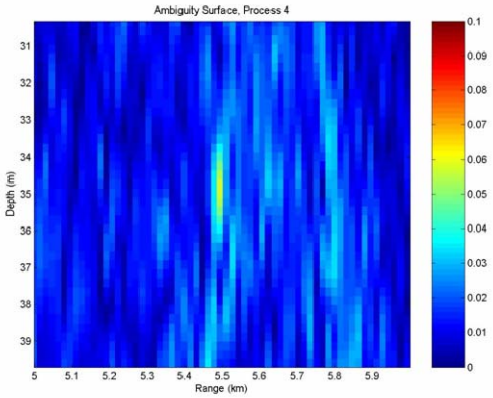

Figure 39. AMS plot for pressure only at 5 km, 1000 Hz, with no perturbation

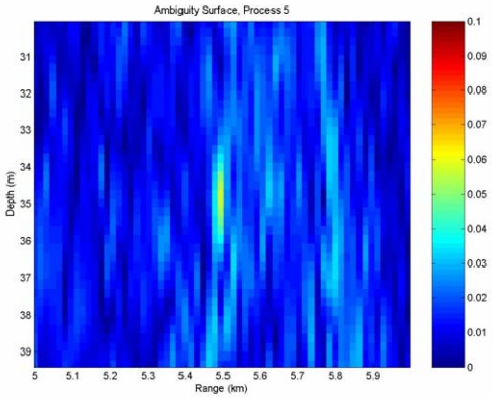

Figure 40. AMS plot for equal weighting of p, v_r and v_z at 5 km, 1000 Hz, with no perturbation

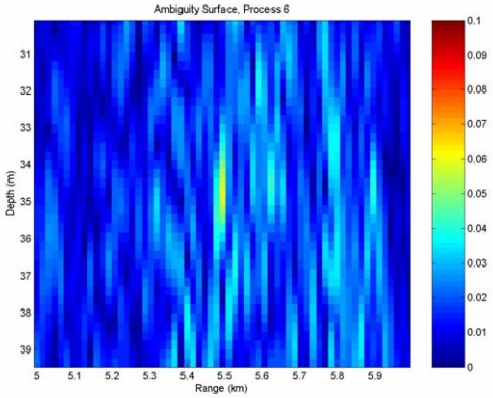

Figure 41. AMS plot for equalized weightings of p, v_r and v_z at 5 km, 1000 Hz, with no perturbation

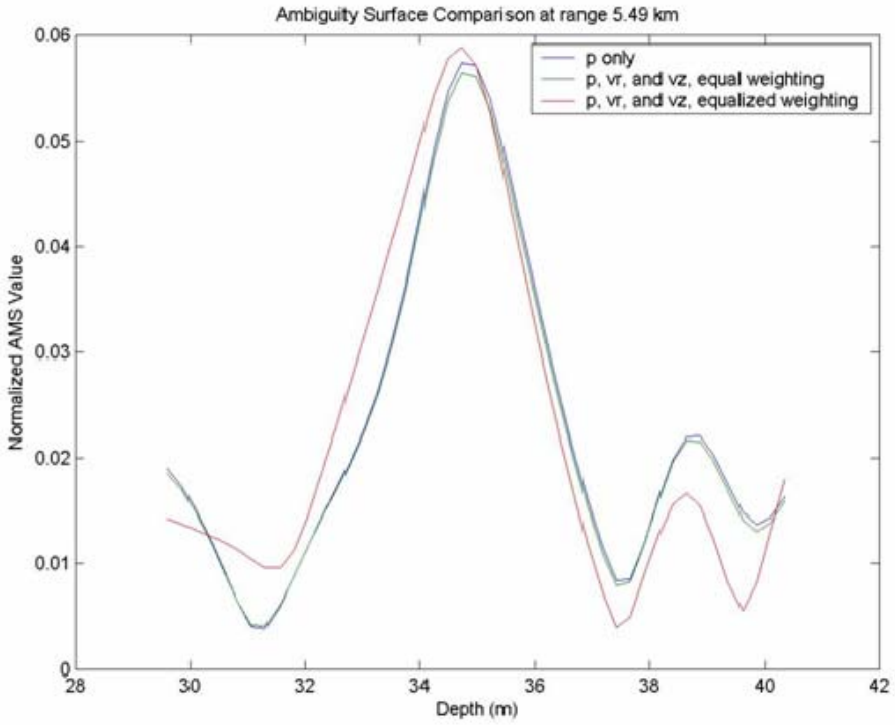

Figure 42. Normalized AMS value vs. depth plot at range 5.49 km

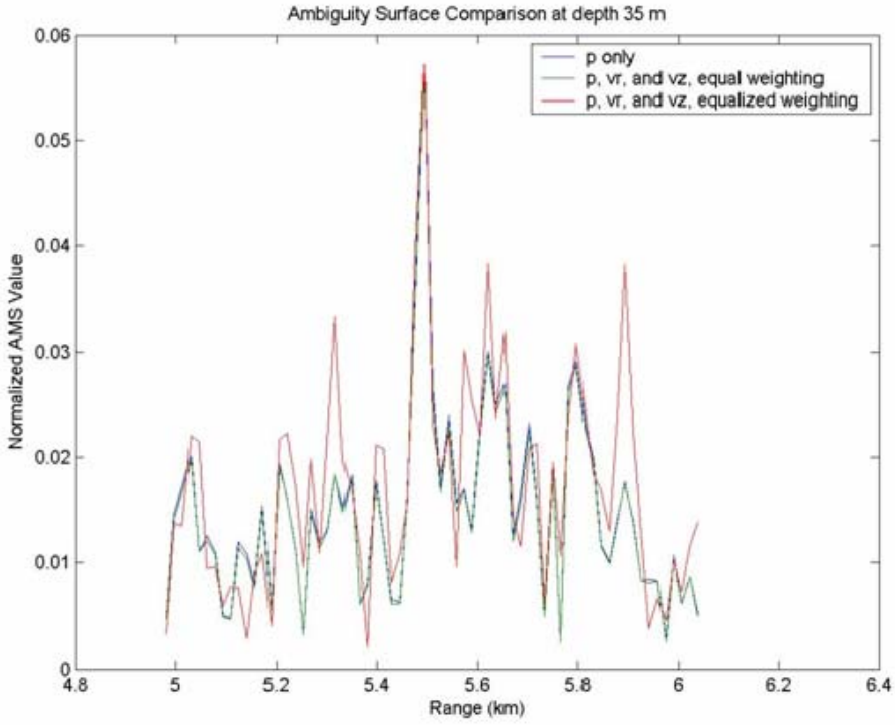

Figure 43. Normalized AMS value vs. range plot at depth 35 m

b) Mixed Layer 150 m, 10 km, 1000 Hz, no Perturbation

Comparing the AMS plots (Figs. 44-46) computed from the respective weightings of data, it is observed that all three plots have the source clearly localized at the correct position, without any apparent difference in strength. Comparing the variability of the ambiguity surfaces, it is obvious again that the equalized weight AMS plot has the highest level, while that of the other two plots are similar. Figure 47 provides the normalized AMS values at range 11.02 km (known source range) against depth while Fig. 48 provides the normalized AMS values at depth 35 m (known source depth) against range. These two plots reinforce the observations made from Figs. 44-46.

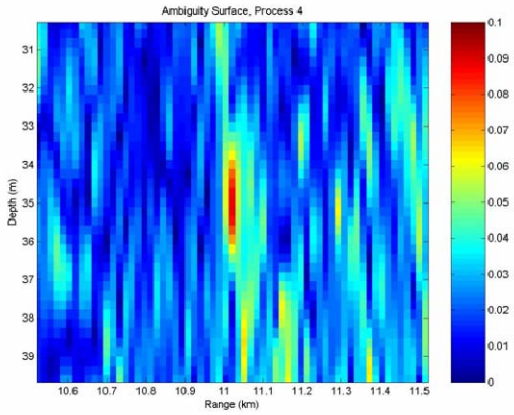

Figure 44. AMS plot for pressure only at 10 km, 1000 Hz, with no perturbation

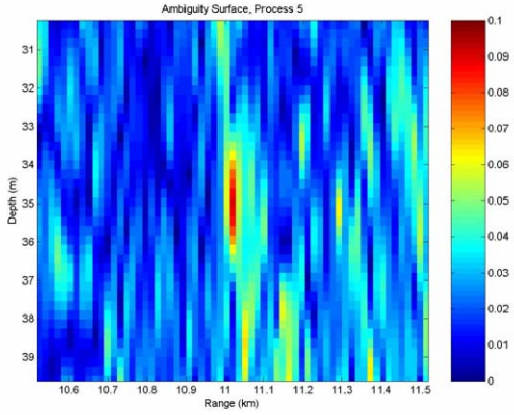

Figure 45. AMS plot for equal weighting of p, v_r and v_z at 10 km, 1000 Hz, with no perturbation

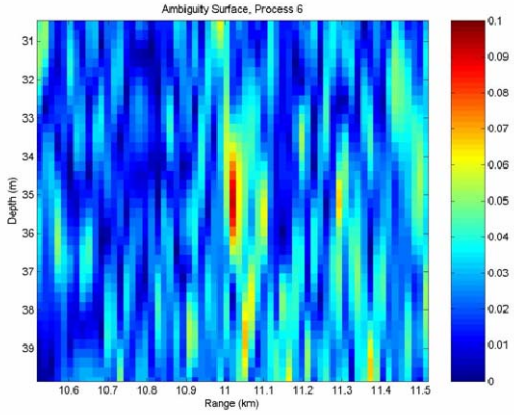

Figure 46. AMS plot for equalized weightings of p, v_r and v_z at 10 km, 1000 Hz, with no perturbation

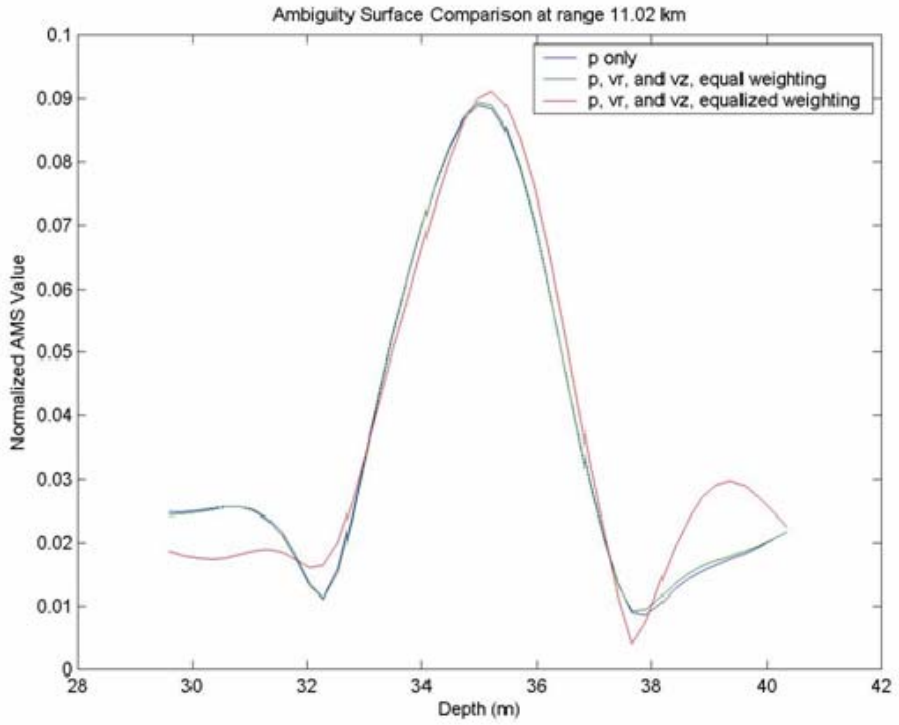

Figure 47. Normalized AMS value vs. depth plot at range 11.02 km

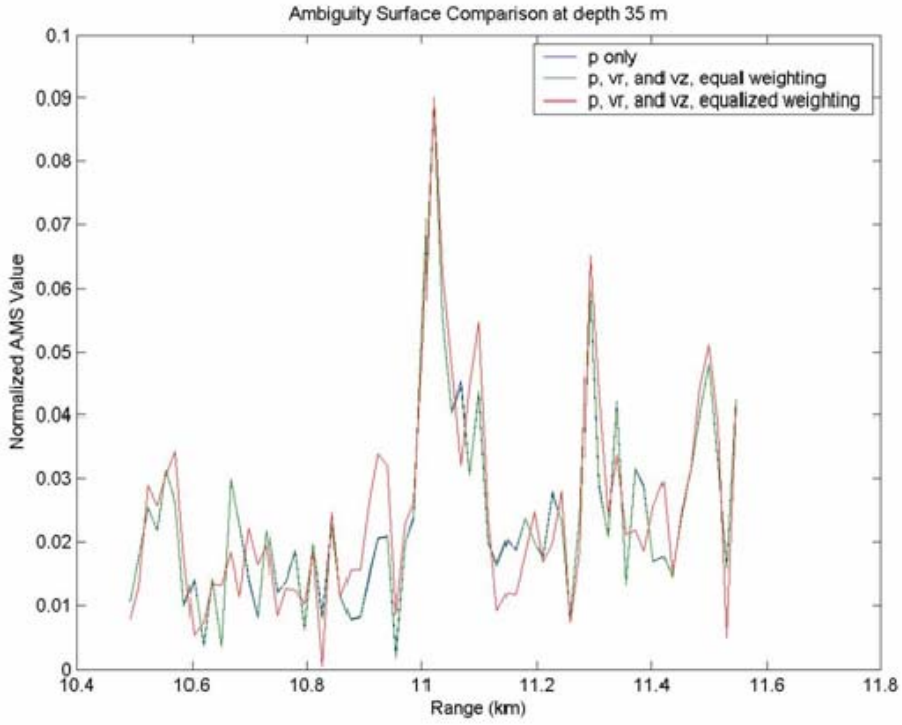

Figure 48. Normalized AMS value vs. range plot at depth 35 m

c) Mixed Layer 150 m, 15 km, 1000 Hz, no Perturbation

Comparing the AMS plots (Figs. 49-51) computed from the respective weightings of data, it is observed that all three plots have the source fairly well localized at the correct position though the variability of the ambiguity surfaces is very high for all three cases. The equalized weighting AVS data has the highest level of ambiguity followed by the pressure only data. Figure 52 provides the normalized AMS values at range 15.42 km (known source range) against depth while Fig. 53 provides the normalized AMS values at depth 35 m (known source depth) against range. Figure 52 displays two strong peaks at 35 m and 38 m depth while Fig. 53 also displays a few high peaks that reinforce the observations from Figs. 49-51.

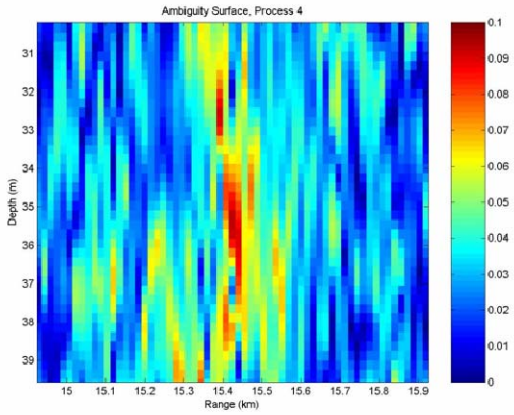

Figure 49. AMS plot for pressure only at 15 km, 1000 Hz, with no perturbation

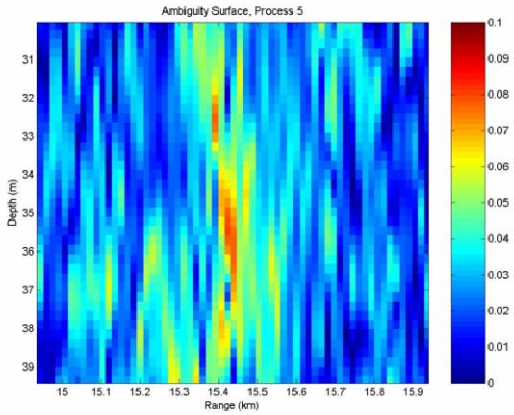

Figure 50. AMS plot for equal weighting of p, v_r and v_z at 15 km, 1000 Hz, with no perturbation

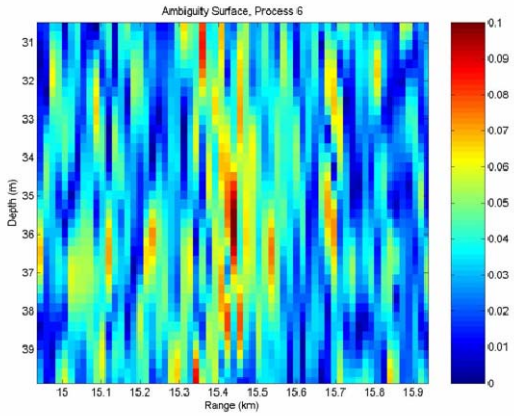

Figure 51. AMS plot for equalized weightings of p, v_r and v_z at 15 km, 1000 Hz, with no perturbation

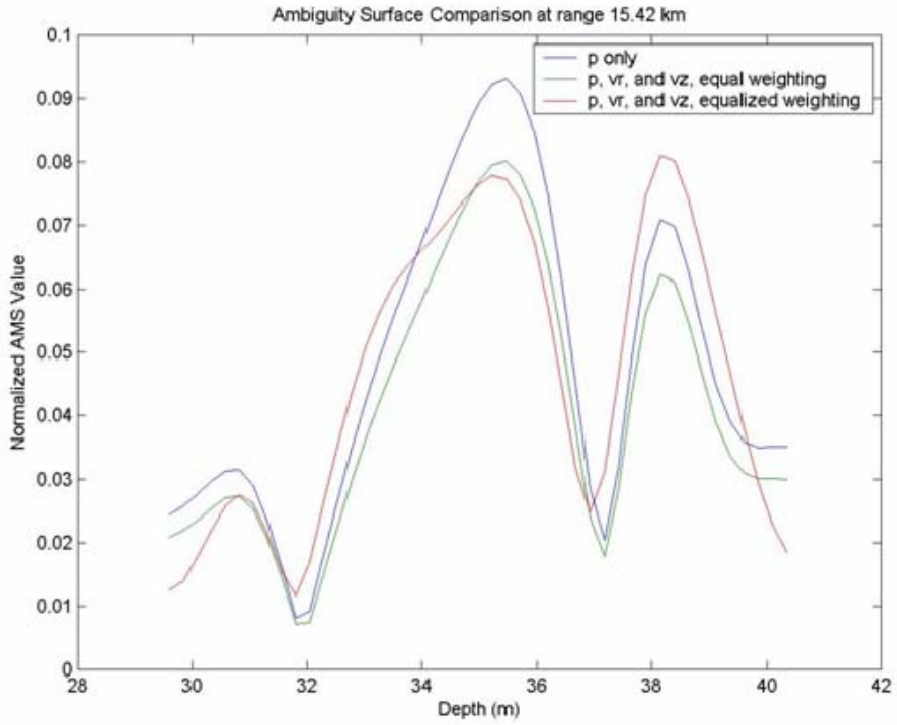

Figure 52. Normalized AMS value vs. depth plot at range 15.42 km

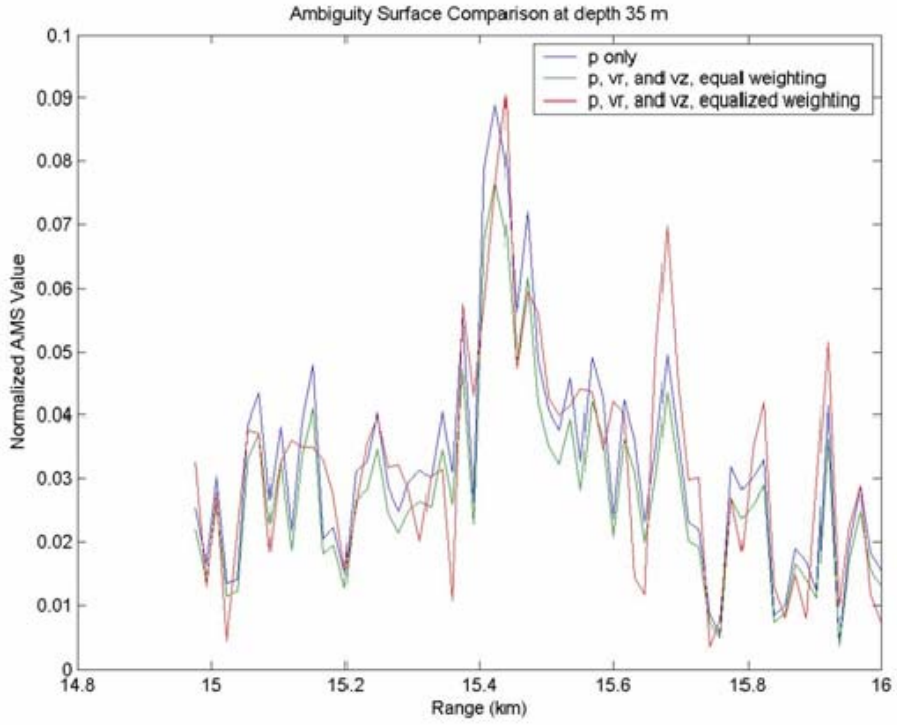

Figure 53. Normalized AMS value vs. range plot at depth 35 m

d) Mixed Layer 150 m, 5 km, 1000 Hz, Interface Roughness

Comparing the AMS plots (Figs. 54-56) computed from the respective weightings of data, it is observed that all three plots are unable to localize the source. All three plots also have very low levels of variability. Figure 57 provides the normalized AMS values at range 5.49 km (known source range) against depth while Fig. 58 provides the normalized AMS values at depth 35 m (known source depth) against range. These two plots reinforce the observations made from Figs. 54-56.

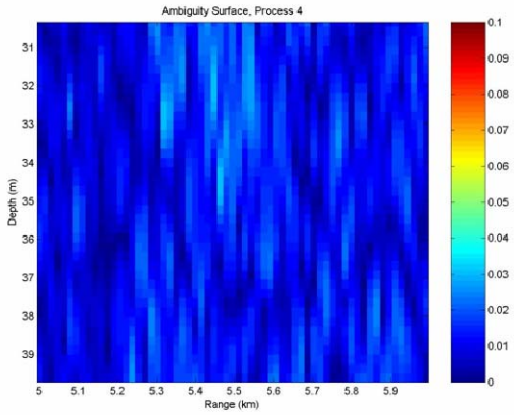

Figure 54. AMS plot for pressure only at 5 km, 1000 Hz, with interface roughness

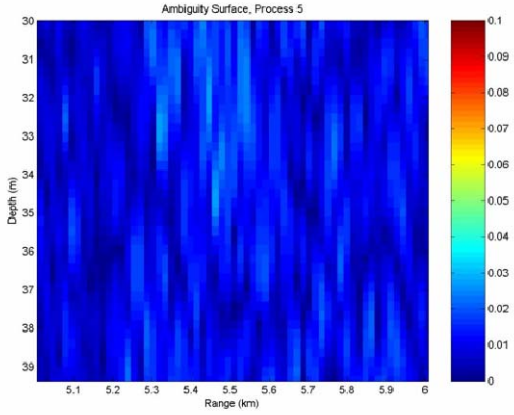

Figure 55. AMS plot for equal weighting of p, v_r and v_z at 5 km, 1000 Hz, with interface roughness

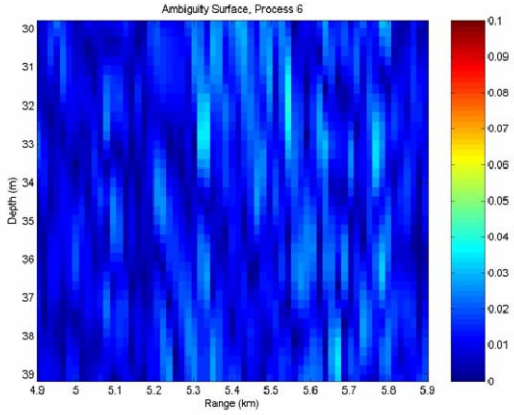

Figure 56. AMS plot for equalized weightings of p, v_r and v_z at 5 km, 1000 Hz, with interface roughness

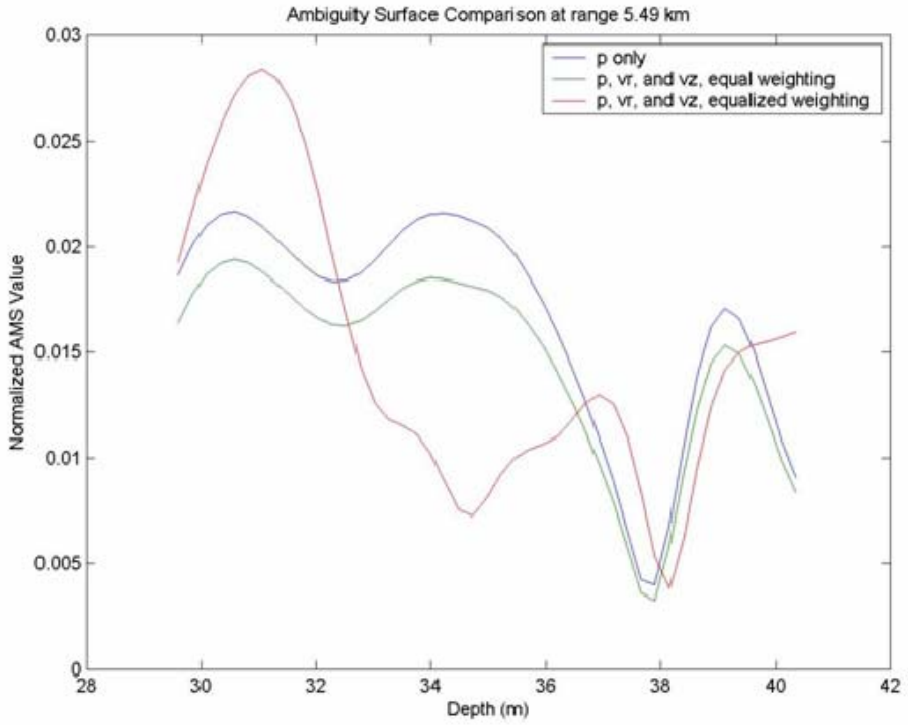

Figure 57. Normalized AMS value vs. depth plot at range 5.49 km

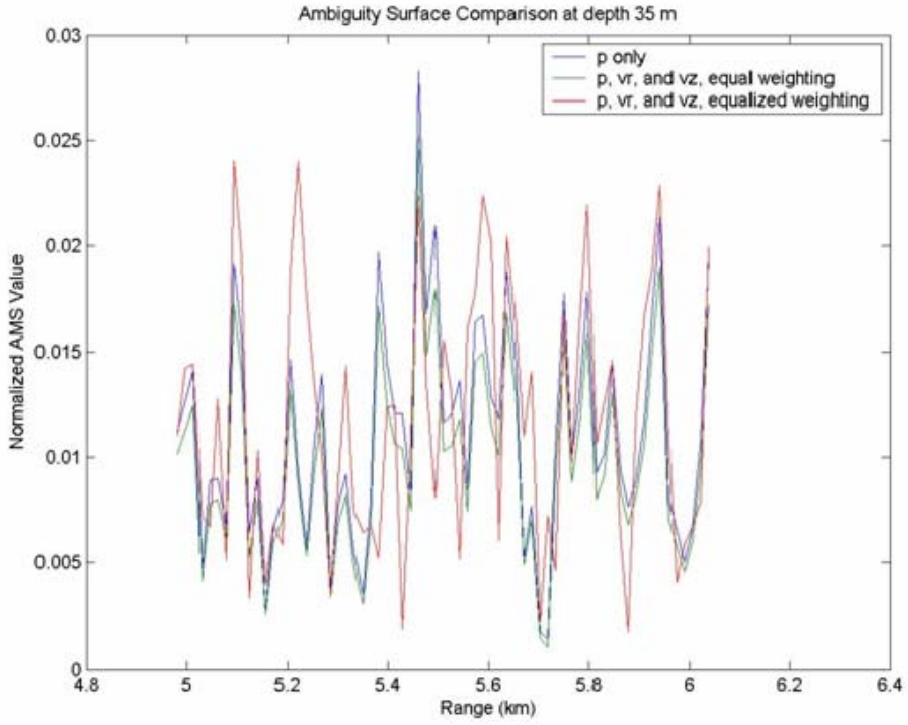

Figure 58. Normalized AMS value vs. range plot at depth 35 m

e) Mixed Layer 150 m, 10 km, 1000 Hz, Interface Roughness

Comparing the AMS plots (Figs. 59-61) computed from the respective weightings of data, it is observed that all three plots are unable to localize the source. All three plots also have low levels of variability in the ambiguity surfaces. Figure 62 provides the normalized AMS values at range 11.02 km (known source range) against depth while Fig. 63 provides the normalized AMS values at depth 35 m (known source depth) against range. These two plots reinforce the observations made from Figs. 59-61.

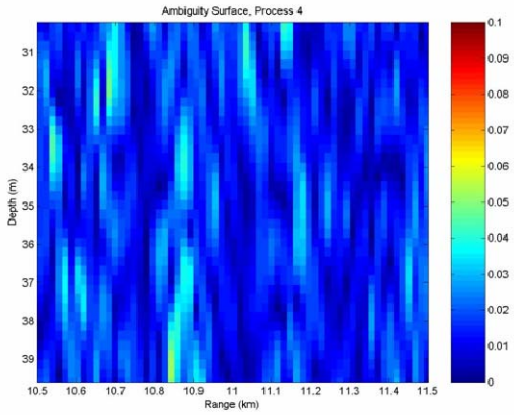

Figure 59. AMS plot for pressure only at 10 km, 1000 Hz, with interface roughness

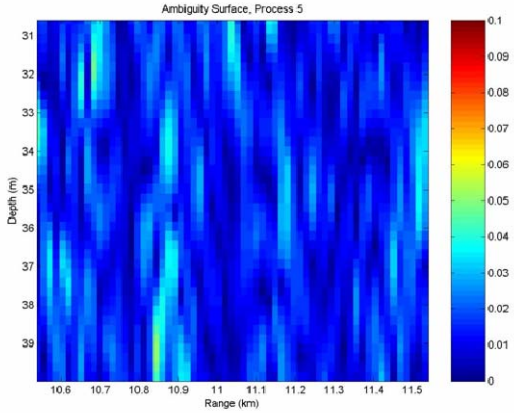

Figure 60. AMS plot for equal weighting of p, v_r and v_z at 10 km, 1000 Hz, with interface roughness

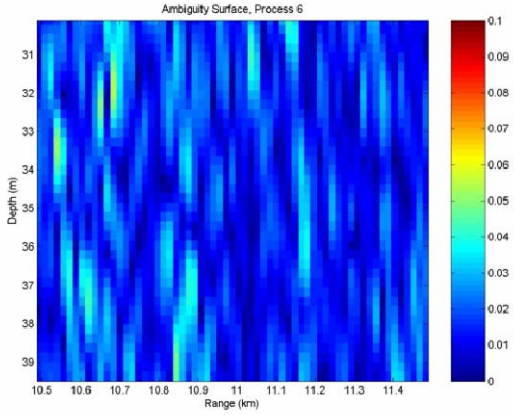

Figure 61. AMS plot for equalized weightings of p, v_r and v_z at 10 km, 1000 Hz, with interface roughness

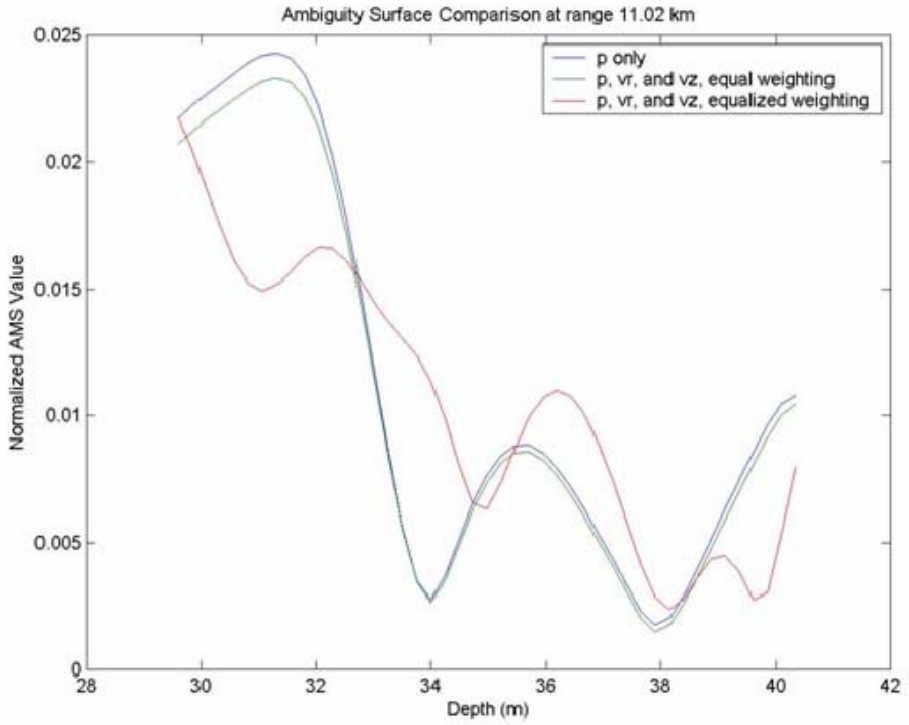

Figure 62. Normalized AMS value vs. depth plot at range 11.02 km

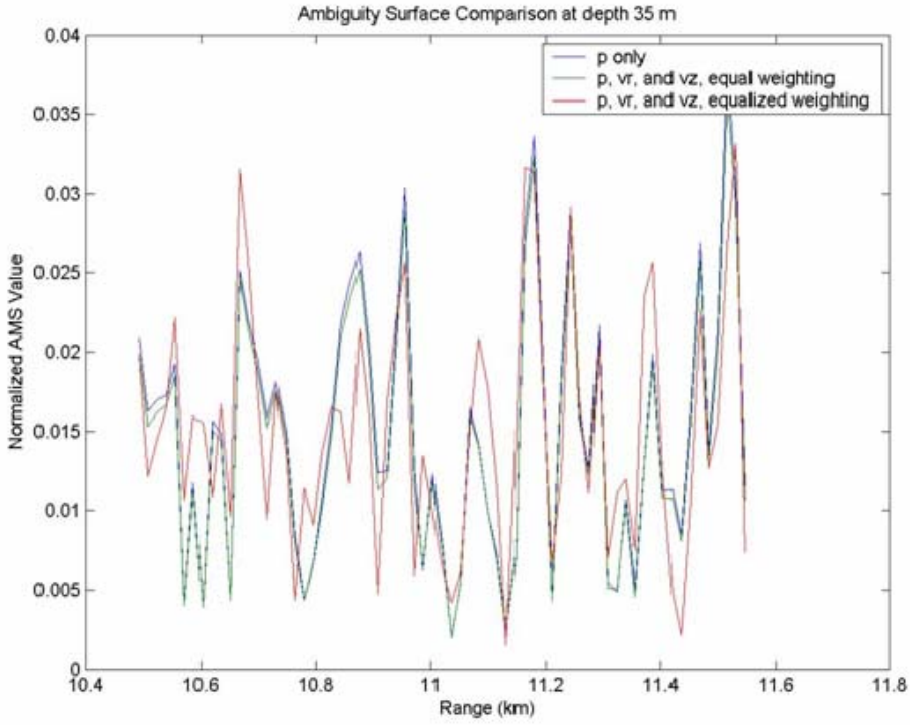

Figure 63. Normalized AMS value vs. range plot at depth 35 m

f) Mixed Layer 150 m, 15 km, 1000 Hz, Interface Roughness

Comparing the AMS plots (Figs. 64-66) computed from the respective weightings of data, it is observed that all three plots were able to localize the source at 15.38 km range, 34 m depth, which was not the known source position. All three plots also have fairly low levels of ambiguity variability with the equalized weighting AVS having the highest. Figure 67 provides the normalized AMS values at range 15.42 km (known source range) against depth while Fig. 68 provides the normalized AMS values at depth 35 m (known source depth) against range. Figure 67 displays two peaks at 36 m and 39 m depth while Fig. 68 displays a peak at 15.38 km with equalized weighting AVS data displaying a distinctly higher value at this peak compared to the rest.

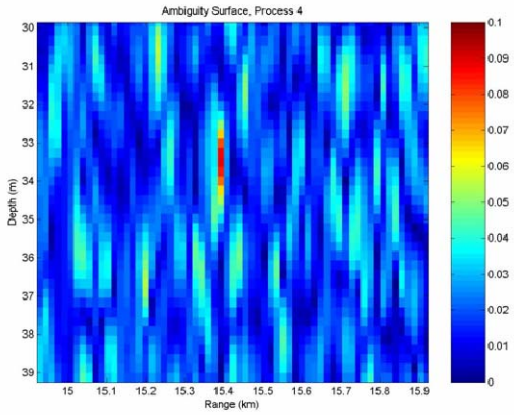

Figure 64. AMS plot for pressure only at 15 km, 1000 Hz, with interface roughness

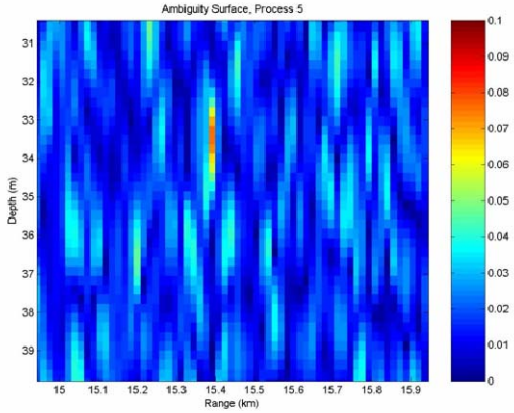

Figure 65. AMS plot for equal weighting of p, v_r and v_z at 15 km, 1000 Hz, with interface roughness

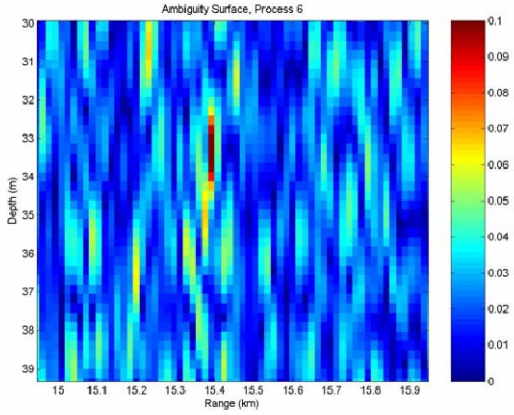

Figure 66. AMS plot for equalized weightings of p, v_r and v_z at 15 km, 1000 Hz, with interface roughness

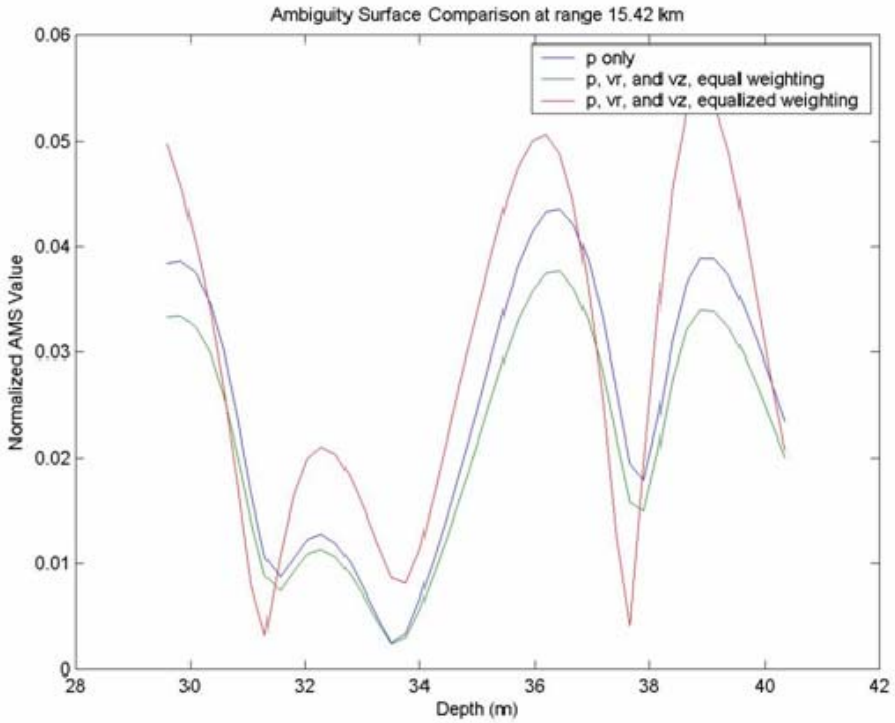

Figure 67. Normalized AMS value vs. depth plot at range 15.42 km

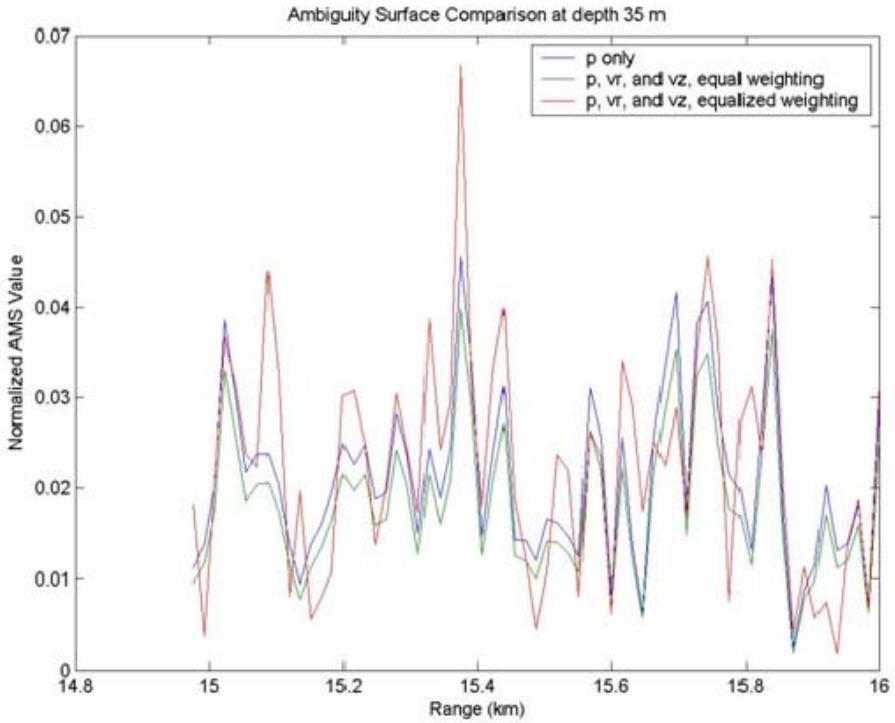

Figure 68. Normalized AMS value vs. range plot at depth 35 m

3. Summary of Results

The performance of a hydrophone array and an AVS array were compared based on Ambiguity Surface plots as a function of source depth and range. These plots were assessed based on their ability to pinpoint the correct source location and their variability which could result in incorrect source localizations. After comparing all the AMS plots, a summary of observations is as follows:

- In the Pekeris 150 m environment with no perturbation (Figs. 9-23), it appeared that the equalized weighting AVS array performed the worst as it consistently produced the highest variability compared to the other two. The performances for the hydrophone array and equal weighting AVS array seemed very similar except between Figs. 9 and 10 where the hydrophone array plot appeared to have a both a stronger signal at the correct location and a higher level of variability while the equal weighting array appeared to have a weaker signal with lower level of variability.

- In the Mixed Layer 150 m environment with no perturbation (Figs. 39-53), it appeared again consistently that the equalized weighting AVS array performed the worst compared to the other two. The performances between the hydrophone array and equal weighting AVS array seemed similar again except for Figs. 49 and 50 where the plot for the hydrophone array appeared to have a higher level of variability.

- Where interface roughness was applied for either of the environments, it was observed that incorrect localization was achieved for three cases: Pekeris 150 m at 5 km (Figs. 24-28), Pekeris 150 m at 15 km (Figs. 34-38) and Mixed Layer 150 m at 15 km (Figs. 64-68). These localizations were achieved by all three types of sensor data. It is thought that this could have occurred through scattering caused by the introduction of interface roughness. In Figs 64-68 where the range applied was 15 km in the Mixed Layer 150 m environment, source localization was achieved by all three arrays very close to the exact position of 35 m depth, 15.42 km range. It is believed that this detection was possible (while nearer runs were not) due

to the close proximity to caustic zones for the surface channel. Based on this detection, it was assessed that the hydrophone and equal weighting AVS array performed equally well while the equalized weighting AVS array was slightly inferior due to higher level of variability near the detection.

Based on this work hydrophone arrays using matched field processing to localize an acoustic source are expected to perform as well as AVS arrays using an equal weighting of all components. AVS arrays using equalized weightings were prone to high levels of variability in the calculated Ambiguity Surface and are, therefore, more likely to lead to incorrect localizations. None of the methods worked reliably in the presence of perturbations.

THIS PAGE INTENTIONALLY LEFT BLANK

V. CONCLUSIONS

A. SUMMARY OF ACHIEVEMENTS

The summary of achievements carried out in this thesis are as follows:

- A MATLAB-based matched-field processor was developed and tested against known theory, confirming its applicability.
- This processor was then applied to produce the Ambiguity Surface (AMS) plots used to compare the performances of hydrophone and AVS arrays using acoustic field information simulated by the MMPE model.
- A simple analysis on the performances by hydrophone and AVS arrays was provided, implying that the hydrophone array performed as well as the AVS array based on the component weightings examined in this study.

In applying the MATLAB-based correlator processor with incoming plane waves as well as MMPE simulated acoustic data, the maximum gain achieved by the optimal weightings AVS array over the hydrophone array was 6 dB, consistent with theoretical analysis stated in [5]. The performance of equal weighting AVS array was also observed to be better than the hydrophone array as expected.

When applying the processor to MFP tests using MMPE simulated data, the performances of hydrophone and AVS arrays were compared based on AMS plots as well as AMS normalized-value plots at known source range and depth. The localizations of source location through MFP performed within expectations, according to the varied environments and perturbations, lending credence that the comparisons were fairly dependable.

Through this simple analysis, it was concluded that the performance of a hydrophone array is comparable to that of the AVS array in the context of linear, matched-field processing. However, other variables (different perturbations, different weightings, adaptive processors, etc) were not tested, and so these results should be considered very limited.

B. FUTURE WORK

The issue of whether AVS arrays can outperform hydrophone arrays is far from settled based on this thesis, though a certain insight was provided for the case of matched field processing. Much more work is required to compare the performance for different processing algorithms and environmental conditions. Further research is also required to determine the reasons behind any differences in performance. This is an area of research that can potentially benefit many industries associated with the underwater domain.

LIST OF REFERENCES

[1] Malcolm Hawkes and Arye Nehorai, "Acoustic Vector-Sensor Correlations in Ambient Noise," IEEE J. of Ocean. Eng., **26**, pp 337-347 (2001).

[2] Arye Nehorai and Eytan Paldi, "Acoustic Vector-Sensor Array Processing," IEEE Trans. on Signal Proc., **42**, pp 2481-2491 (1994).

[3] Finn B. Jensen, William A. Kuperman, Michael B. Porter and Henrik Schmidt, "Computational Ocean Acoustics," AIP Press, 2000.

[4] Alexander Tolstoy, "Matched Field Processing for Underwater Acoustics," World Scientific Publishing, 1993.

[5] Benjamin A. Cray and Albert H. Nuttall, "Directivity Factors for Linear Arrays of Velocity Sensors," J. Acoust. Soc. Am., **110**, pp. 324-331 (2001).

[6] G. L. D'Spain, W. S. Hodgkiss and G. L. Edmonds, "Energetics of the deep ocean's infrasonic Sound Field," J. Acoust. Soc. Am. **89**, pp. 1134-1158 (1991).

[7] Kevin B. Smith, "Modeling and multipath phenomenology of acoustic particle velocity fields in shallow water environments," J. Acoust. Soc. Am. (2005, submitted).

[8] K. B. Smith and F. D. Tappert, "UMPE: The University of Miami Parabolic Equation Model, Version 1.0," Marine Physical Laboratory Technical Memo 432, 1993.

[9] Kevin B. Smith, "The MMPE Underwater Acoustic Propagation Model and Some Applications," powerpoint presentation given at Naval Postgraduate School on 21 Nov 2003.

[10] Kevin B. Smith, "Convergence, Stability, and Variability of Shallow Water Acoustic Predictions Using a Split-Step Fourier Parabolic Equation Model," J. of Comp. Acoust., **9**, pp243-285 (2001).

[11] R. H. Hardin and F. D. Tappert, “Applications of the split-step Fourier method to the numerical solution of nonlinear and variable coefficient wave equations,” SIAM Rev. **15**, 423 (1973).

[12] D. J. Thomson and N.R. Chapman, “A wide-angle split-step algorithm for the parabolic equation,” J. Acoust. Soc. Am. **74**, pp. 1848-1854 (1983).

[13] Robert J. Urick, “Principles of Underwater Sound, 3rd Edition,” Peninsula Publishing, 1983.

[14] Robert M. Hill, “Model-data comparison of shallow water acoustic reverberation in the East China Sea,” Master’s Thesis, Naval Postgraduate School, Monterey, CA, September 2003.

INITIAL DISTRIBUTION LIST

1. Defense Technical Information Center
   Ft. Belvoir, Virginia

2. Dudley Knox Library
   Naval Postgraduate School
   Monterey, California

3. Professor Kevin Smith
   Physics Department
   Naval Postgraduate School
   Monterey, California

4. Professor Daphne Kapolka
   Physics Department
   Naval Postgraduate School
   Monterey, California

5. Professor Yeo Tat Soon
   Temasek Defence Systems Institute
   Singapore

6. Ms Tan Lai Poh
   Temasek Defence Systems Institute
   Singapore

7. MAJ Hsu Yu Chih
   Republic of Singapore Navy
   Singapore